



# Corrosion characterization and ion release in SLM-manufactured and wrought Ti6Al4V alloy in an oral environment

Mirjam Bajt Leban<sup>a</sup>, Tadeja Kosec<sup>a,\*</sup>, Matjaž Finšgar<sup>b</sup>

<sup>a</sup> Slovenian National Building and Civil Engineering Institute, Dimičeva ulica 12, SI-1000 Ljubljana, Slovenia

<sup>b</sup> University of Maribor, Faculty of Chemistry and Chemical Engineering, Smetanova ulica 17, SI-2000 Maribor, Slovenia

## ARTICLE INFO

**Keywords:**  
Ti6Al4V  
SLM  
Corrosion  
Ion release  
XPS  
ToF-SIMS

## ABSTRACT

As-produced and heat-treated TiAlV samples were prepared by selective laser melting and compared to wrought samples of identical chemical composition. Microstructural, corrosion, and spectroscopic studies of additively manufactured samples in artificial saliva at 37 °C, with NaF and at pH 2.3 were as a novelty combined with metal ion release during 42 days immersion. In artificial saliva higher amount of ions was released on SLM specimen when compared to wrought alloy. The total amount of ions released from SLM specimen in AS containing NaF was 10-times higher than in AS, while in AS with lactic acid it was 100-times higher.

## 1. Introduction

Titanium and its alloys have been successfully used for decades as critical components in aerospace and the energy industry. Because of their exceptional corrosion resistance and biocompatibility, they are also commonly used for orthopedic and dental implants and prosthodontic treatments. In addition to commercially-available pure titanium grades (Ti-CP), various titanium alloys can also be used for these purposes. The titanium alloy most commonly used and studied is Ti6Al4V, which has a higher strength than Ti-CP while maintaining comparable corrosion resistance and biocompatibility properties. Al and V, the main alloying elements of Ti6Al4V, are, however, subject to health concerns, since they have been reported to cause health problems including allergic reactions, carcinogenic and neurological disorders [1–5]. The most common problem associated with using this type of titanium alloy is peri-implantitis, which, according to several studies [1,6–8], could affect a significant proportion of patients [9]. Peri-implantitis is triggered by an inflammatory process that affects the tissue around an implant, causing the resorption and loss of bone. An increased number of metal particles and ions has been found in the vicinity of such tissue damage [8,9]. Ions released from metal implants in contact with tissue, bone, bodily fluids or an oral environment could decrease osteoblastic cell viability [10] and induce cytotoxic effects [5]. A systematic review of the potential causes of titanium particles and ion release in implant dentistry [11] listed past clinical studies conducted on animals that have confirmed the presence of metal particles in inflamed tissue.

The particles of titanium alloy have been shown to originate from mechanical or chemical attacks that occur either during the surgical procedure used to insert the implant, or during its maintenance [11,12], causing various types of corrosion and impacting the lifespan of the implant [13]. Corrosion processes that occur on the metal implant–tissue or oral environment interface cause the release of metal ions via both direct dissolution of the alloy and through the interaction of the passive film with the oral environment [7]. Tribocorrosion comprises a combined effect of metal removal by wear and chemical oxidation of freshly exposed area to saliva or air and accelerates the overall ion release process [12,14]. A passive film instantaneously forms on a TiAlV alloy following exposure to an oxygen-containing environment, which is crucial for corrosion resistance in the harsh oral environment [1]. Saliva presents a near neutral environment [15] containing corrosive ions, to which additional chlorides and fluorides from tooth care products (toothpaste or mouthwashes) can be added. The pH level can decrease as a result of inflammatory processes and dietary uptake, and consequently the protective properties of the titanium passive layer deteriorate. Corrosion can therefore be autocatalytically driven by the inflammatory process. In artificial saliva (AS), at human body temperature, fluoride ions interact with hydrogen ions producing a slightly acidic local environment [16]. This subsequently deteriorates the passive layer on the TiAlV, which is primarily composed of homogenous TiO<sub>2</sub>, with minor amounts of the less stable Al<sub>2</sub>O<sub>3</sub> and V<sub>2</sub>O<sub>5</sub> [17]. On the other hand, AS acidified by the addition of lactic acid has been shown to cause dissolution of the passive film and pitting corrosion [18].

\* Corresponding author.

E-mail address: [tadeja.kosec@zag.si](mailto:tadeja.kosec@zag.si) (T. Kosec).

<https://doi.org/10.1016/j.corsci.2022.110716>

Received 23 June 2022; Received in revised form 15 September 2022; Accepted 1 October 2022

Available online 4 October 2022

0010-938X/© 2022 The Author(s). Published by Elsevier Ltd. This is an open access article under the CC BY-NC-ND license (<http://creativecommons.org/licenses/by-nc-nd/4.0/>).

The crucial roles of passivation and corrosion behaviour are determined by the chemistry of the alloy and its microstructural composition. TiAlV is an  $\alpha + \beta$  alloy. These alloys can be produced in a variety of ways, including by casting, forging, through the wrought process and using various additive manufacturing techniques. Thermal and thermo-mechanical treatments are applied either as part of the production process or following production, primarily in order to improve the mechanical properties of the end product [19,20]. These processes lead to differing microstructures; in the case of production by casting, for example, the microstructure is lamellar, forging with post-solution heat-treatment results in an equiaxed microstructure, and selective laser melting (SLM), one of the most commonly used additive manufacturing techniques, leads to a martensitic microstructure as a result of the fast cooling rates [21,22]. In a lamellar  $\alpha + \beta$  microstructure, the homogeneity of the passive film developed above these phases has been shown to differ, due to the difference in solubility of the stabilizing elements (Al for  $\alpha$  and V for  $\beta$ ) [23]. It is reported that this difference between the chemical composition of lamellas might cause corrosion as a result of the galvanic effect [1]. A martensitic microstructure, characteristic of TiAlV alloy produced by SLM, contains alpha prime martensite ( $\alpha'$ ), which enables the formation of a more homogeneous and stable passive film, and consequently alloys of this type have better corrosion resistance than those with a lamellar microstructure [24].

The work provides information on the safe use of Ti6Al4V using additive technologies, such as selective laser melting. For this purpose, tests on ion release according to standard ISO 10271:2011 Dentistry — Corrosion test methods for metallic materials were performed in combination with corrosion measurements and surface analyses of the passive film formed in AS with or without the addition of fluoride ions and lactic acid. Samples using additive technologies were compared to wrought alloys, on which most of the research has been carried out previously.

The present study aims to compare the corrosion resistance of three Ti6Al4V dental alloys with identical chemical compositions but produced in different ways; by SLM without heat treatment, by SLM with heat treatment, and through the wrought process. The electrochemical properties and ion release were determined during 42 days of immersion in AS, AS with the addition of fluoride ions, and AS with lactic acid (to simulate potential inflammatory conditions). Special attention was given to studying the quantities and ratios of alloying elements in the immersion tests and the relationships with their alloy microstructures. Furthermore, surface analysis using X-ray photoelectron spectroscopy (XPS), and time-of-flight secondary ion mass spectrometry (ToF-SIMS) were performed in order to determine any differences in the structure of the passive film on the Ti6Al4V alloy in the various test environments. Finally, atomic force microscopy (AFM) was performed for topography measurements of the exposed samples.

## 2. Materials and methods

### 2.1. Samples

Ti6Al4V alloys were provided by S&S Scheftner GmbH in the form of powder and a wrought milling disc, with respective chemical compositions of 89 wt% Ti, 6 wt% Al, 4 wt% V, and < 1 wt% N, C, H, Fe, and O (Starbond Ti4Powder 45) and 89.4 wt% Ti, 6.2 wt% Al, 4.0 wt% V, and < 0.4 wt% of N, C, H, Fe and O (Starbond Ti5 Disc). Samples were 3D printed from powder using SLM with the following printing parameters: laser power of 75 W, laser travel velocity of 520 mm/s, a hatch distance of 25  $\mu\text{m}$ , and a layer thickness of 25  $\mu\text{m}$ . Namely, during pre-study, where several different parameters were tested, the lowest porosity was obtained with the above given parameters. The printing strategy used was a paintbrush (Fig. 1). The energy density calculated was 230.8 J/mm<sup>3</sup>. Part of the 3D printed samples was also heat treated at 800 °C for 1 h under the protective atmosphere of argon, then cooled to 500 °C

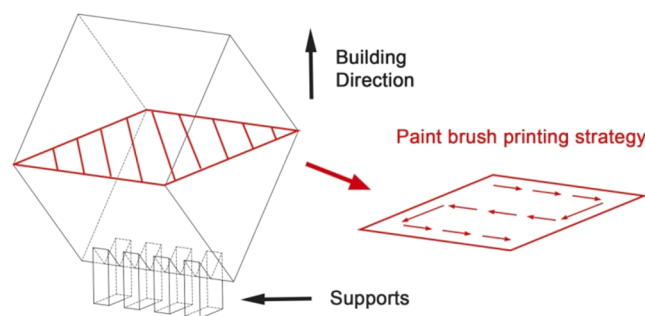


Fig. 1. Printing strategy for SLM building of Ti6Al4V alloy.

in the furnace, followed by air cooling to obtain optimal mechanical properties as suggested previously [19,20,23]. In addition, a part of the samples for tests was extracted from the milling disc by CAD/CAM milling. From hereon, the 3D printed samples are denoted as Ti6Al4V - SLM, the heat-treated 3D printed samples as Ti6Al4V - SLM-HT, and the samples extracted from the wrought milling disc as Ti6Al4V - WR. All types of samples were fabricated in two different shapes: 1) as cubes with an edge length of 8 mm for the electrochemical tests, and 2) as 10 mm diameter cylinders with a height of 30 mm and a total exposed area of 11 mm<sup>2</sup> for the immersion tests.

### 2.2. Microstructural analysis

In order to reveal the microstructures, the metallographic investigation was performed on all three types of samples in two directions: in the case of the SLM disc, both parallel and transverse to the 3D building direction, and on the samples extracted from the milling disc in the transverse direction with respect to the disc axis. The samples were ground and polished with 50 mL 0.06  $\mu\text{m}$  colloidal silica and 10 mL H<sub>2</sub>O<sub>2</sub> (30 vol%). Mirror-polished samples were then etched with Kroll reagent (100 mL water, 3 mL conc. HF, and 6 mL conc. HNO<sub>3</sub>). Observation of the microstructures was conducted using a Zeiss Axio Imager Z2m microscope with Zen software (Carl Zeiss AG, Germany) using bright field light. Field emission scanning electron microscopy (FE-SEM) examination of non-etched and polished specimens was performed by using Zeiss ULTRA plus device (Carl Zeiss AG, Germany). X-ray diffraction (XRD) analysis was carried out using an Empyrean XRD diffractometer (PANalytical, Malvern, UK), and the XRD data were analyzed using HighScore Plus database software. XRD spectra were measured under 4° and 100° (2 $\theta$ ) with a step size of 0.0065° and time per step of 61.2 ms.

### 2.3. Electrochemical tests and immersion tests

Both the electrochemical and the immersion tests were performed in three different saliva-simulating solutions at a human body temperature of 37 °C. AS contained 0.6 g/L NaCl, 0.72 g/L KCl, 0.22 g/L CaCl<sub>2</sub>·0.2 H<sub>2</sub>O, 0.68 g/L KH<sub>2</sub>PO<sub>4</sub>, 0.856 g/L Na<sub>2</sub>HPO<sub>4</sub>·0.12 H<sub>2</sub>O, 0.060 g/L KSCN, 1.5 g/L KHCO<sub>3</sub>, and 0.033 g/L citric acid. AS with the addition of NaF contained 0.315 wt% NaF (0.075 M F<sup>-</sup>), and AS with lactic acid contained 0.1 M lactic acid. The pH of AS and AS with NaF was 6.9  $\pm$  0.1, while the pH of AS with lactic acid was 2.3  $\pm$  0.1.

Two types of electrochemical measurements were conducted: potentiodynamic tests and long-term electrochemical impedance spectroscopy (EIS) measurements. Samples were ground with SiC grinding paper to 1200 grit. Both tests were conducted in a three-electrode corrosion cell, consisting of a working electrode (square samples with an area of 0.64 cm<sup>2</sup> exposed to the solution), a reference electrode (Ag/AgCl(sat. KCl)), and a counter electrode (a graphite rod). First, open circuit potential (OCP) was measured for 6200 s, followed by measurements of linear polarization (LP) (at a scan rate of 0.1 mV/S in the

potential range  $\pm 20$  mV vs OCP) and the potentiodynamic (PD) curve (initial potential of  $-0.25$  mV vs  $E_{\text{corr}}$ , with a potential sweep in the anodic direction up to  $3.50$  V at a scan rate of  $1$  mV/s).

Long-term EIS was performed in the frequency range from  $65$  kHz to  $1$  mHz (7 points per decade) with an AC amplitude of  $\pm 10$  mV (peak-to-peak). EIS measurements were carried out at open circuit potential (OCP) at various times of exposure:  $1$  h,  $4$  h,  $8$  h,  $24$  h,  $48$  h,  $72$  h,  $96$  h,  $120$  h,  $144$  h, and  $172$  h (7 days). Only results at  $24$  h,  $48$  h,  $72$  h,  $120$  h, and  $172$  h were presented in Nyquist and Bode plots together with fitted curves for better clarity. EIS data were fitted using the program Zview (Scribner, Southern Pines, North Carolina, USA) and interpreted based on equivalent electrical circuits. The chi-square values, which represent the goodness of fitting of all the measured data, are given in [Table S1 \(Supplementary\)](#).

The immersion test was conducted according to standard ISO 10271: 2020 (Dentistry — Corrosion test methods for metallic materials) on cylindrical samples inserted into  $15$  mL cuvettes filled with  $11$  mL of testing solution, with a total exposed area of  $11$  cm<sup>2</sup>. Prior to exposure, all samples were blasted with alumina sand of  $105$   $\mu\text{m}$  granulation. Following this surface treatment, the samples were cleaned with ethanol in an ultrasound bath for  $15$  min and then air-dried. The total exposure time during the immersion test was  $42$  days. A fresh solution was placed in the cuvettes on the 1st, 4th, 7th, 14th, 21st, 28th, 35th, and 42nd day of the experiment. Three replicates were exposed to each testing solution using samples of Ti6Al4V - SLM, Ti6Al4V - SLM-HT, and Ti6Al4V - WR. The concentrations of Ti, Al, and V ions in the solution following exposure were measured using an ICP-MS Agilent 7900x (Agilent Technologies, Japan). The concentrations measured were normalized according to the exposed area, such that the results were given as the total amount of released ions per  $1$  cm<sup>2</sup> of the sample exposed.

#### 2.4. XPS, AFM, and ToF-SIMS measurements

The composition of the passive layer formed on the SLM samples after 7 days of exposure to each type of AS at  $37$  °C was analysed by XPS, AFM, and ToF-SIMS.

A Supra+ instrument (Kratos, Manchester, UK) equipped with an Al K $\alpha$  ( $1486.6$  eV) source and a monochromator was used for the XPS measurements. Photoelectrons were acquired at a take-off angle of  $90^\circ$ . A binding energy (BE) scale correction was performed, using the C-C/C-H peak in the C 1s spectrum at  $284.8$  eV for the spectra obtained before sputtering, and the O 1s peak for the spectra obtained during sputtering. High-resolution spectra (before sputtering) were acquired on a 700 by  $300$   $\mu\text{m}$  spot size at a pass energy of  $20$  eV. For depth profiling, pass energies of  $160$  eV and  $40$  eV were used for survey spectra and high-resolution spectra measurements, respectively. A  $2$  by  $2$  mm etch crater was formed by rastering the surface with a  $5$  keV Ar<sup>+</sup> sputter beam. The sputtering rate was determined as  $4$  nm/min, using a reference Ta<sub>2</sub>O<sub>5</sub> sample. The diameter of the analysis area during depth profiling was  $110$   $\mu\text{m}$ , and the emission current was  $15$  mA for both the survey and high-resolution spectra. Data acquisition and processing were performed using 1.4 ESCAPE software (Kratos, Manchester, UK).

An MFP 3D Origin Plus device (Asylum/Oxford Instruments, Santa Barbara, CA, USA) was employed for the AFM measurements. Measurements were performed in tapping mode using an OMCL-AC240TS-R3 silicon cantilever (Olympus Micro Cantilever, Taipei, Taiwan).

ToF-SIMS measurements were performed with an M6 device (ION-TOF, Münster, Germany). Spectra in both polarities were calibrated with peaks of known  $m/z$ . 2D imaging was performed in positive polarity on an analysis area of  $500$  by  $500$   $\mu\text{m}$  using a  $30$  keV Bi<sup>+</sup> primary beam. 3D imaging associated with sputtering was performed with a  $500$  eV Cs<sup>+</sup> sputter beam on an area of  $300$  by  $300$   $\mu\text{m}$ , while analysis was performed using a  $15$  keV Bi<sup>+</sup> primary beam on an analysis area of  $100$  by  $100$   $\mu\text{m}$ . The acquisition and processing of ToF-SIMS data were performed using SurfaceLab 7.3 software.

### 3. Results

#### 3.1. Microstructural analysis

[Fig. 2a-c](#) show the etched microstructures of all three types of samples investigated, Ti6Al4V - SLM, Ti6Al4V - SLM-HT, and Ti6Al4V - WR, respectively. It is clear that different microstructures are developed by the three different methods of production. Characteristic  $\alpha'$  (alpha prime) lamellar martensite with fine acicular morphology can be seen in the microstructure of Ti6Al4V - SLM, developed as a result of the fast cooling rates from the laser melting temperature during 3D printing ([Fig. 2a, e and h](#)).

Heat treatment (Ti6Al4V-SLM-HT) at  $800$  °C, which is below the  $\beta$ -transus temperature ( $998$  °C for Ti6Al4V), yet above the martensite start temperature (around  $650$  °C, [19]), causes transformation of  $\alpha'$  to  $\alpha + \beta$  lamellar microstructure with Widmanstätten morphology [25]. The  $\alpha$ -phase (hexagonal closed packs - hcp) appears in [Fig. 2b and f](#) as bright lamellas on  $\beta$ -grain boundaries (body centered cubic - bcc). On the other hand, in [Fig. 2i](#)  $\alpha$ -phase structure appears as a dark one, and  $\beta$ -phase, which is in between  $\alpha$  lamellas, is a bright one.

The microstructure of the Ti6Al4V-WR sample observed by optical microscope ([Fig. 2c and g](#)) consisted of mixed equiaxed  $\alpha$ -grains (bright) with intergranular  $\beta$  islands (dark) at the  $\alpha$ -grain boundaries [1]. In the FE-SEM image ([Fig. 2j](#)), bright  $\beta$ -phase islands are present on the edges and along  $\alpha$ -grains, which are darker. Such a microstructure is significant for a wrought product that has been additionally solution treated [26,27].

[Fig. 3](#) shows XRD patterns of the Ti6Al4V - SLM, Ti6Al4V - SLM-HT, and Ti6Al4V - WR samples. In the case of SLM only the  $\alpha$ -phase (hcp) is observed. The martensitic phase  $\alpha'$ , which develops as a result of the high cooling rates of the printed object during the solidification process, cannot be distinguished from  $\alpha$  by XRD because the crystallographic structure and lattice parameters are the same, although they can be differentiated metallographically [16,22,28]. The  $\alpha + \beta$  structure was observed for the samples Ti6Al4V - SLM-HT and Ti6Al4V - WR.

#### 3.2. Electrochemical measurements

PD curves for the Ti6Al4V - SLM, Ti6Al4V - SLM-HT, and Ti6Al4V - WR samples in the three different solutions, namely AS, AS with NaF, and AS with lactic acid, are presented in [Fig. 4](#). The electrochemical parameters obtained from electrochemical tests are summarized in [Table 1](#). The PD curves measured for the various Ti6Al4V samples are characteristic of highly passive alloys. The passive current density, i.e. the constant current density in the passive region, was of the order  $4$ – $7$   $\mu\text{A cm}^{-2}$  in all the curves. Low current densities in passive regions were observed even at potentials more positive than  $1.4$  V. Some differences in the electrochemical behaviour of the various Ti6Al4V samples were observed at potentials more positive than  $1.4$  V in relation to the corrosive environment.

In AS, the current density in the anodic region had no current fluctuations in the Ti6Al4V - WR sample. The most significant difference between the samples is the fact that current fluctuations in the anodic part of the PD curves were observed with the Ti6Al4V - SLM and Ti6Al4V - SLM-HT samples. A sharp and steady increase in anodic current was observed with the Ti6Al4V - SLM-HT and Ti6Al4V - SLM samples in AS ([Fig. 4a](#)), while in the case of the Ti6Al4V - WR sample the current increased slowly with increasing potential. In AS with NaF ([Fig. 4b](#)), the difference between the passive region of the PD curves is observed at anodic potentials more positive than  $1.0$  V. In the Ti6Al4V - WR sample the current density remains constant, while in the Ti6Al4V - SLM-HT and Ti6Al4V - SLM samples the current density in the anodic region increases slowly, and fluctuations are observed, similar as in AS. A non-distinctive breakdown potential ( $E_b$ ) was observed in the Ti6Al4V - SLM sample ([Fig. 4b](#)).

In acidified AS, differences in the anodic branch of the PD curve

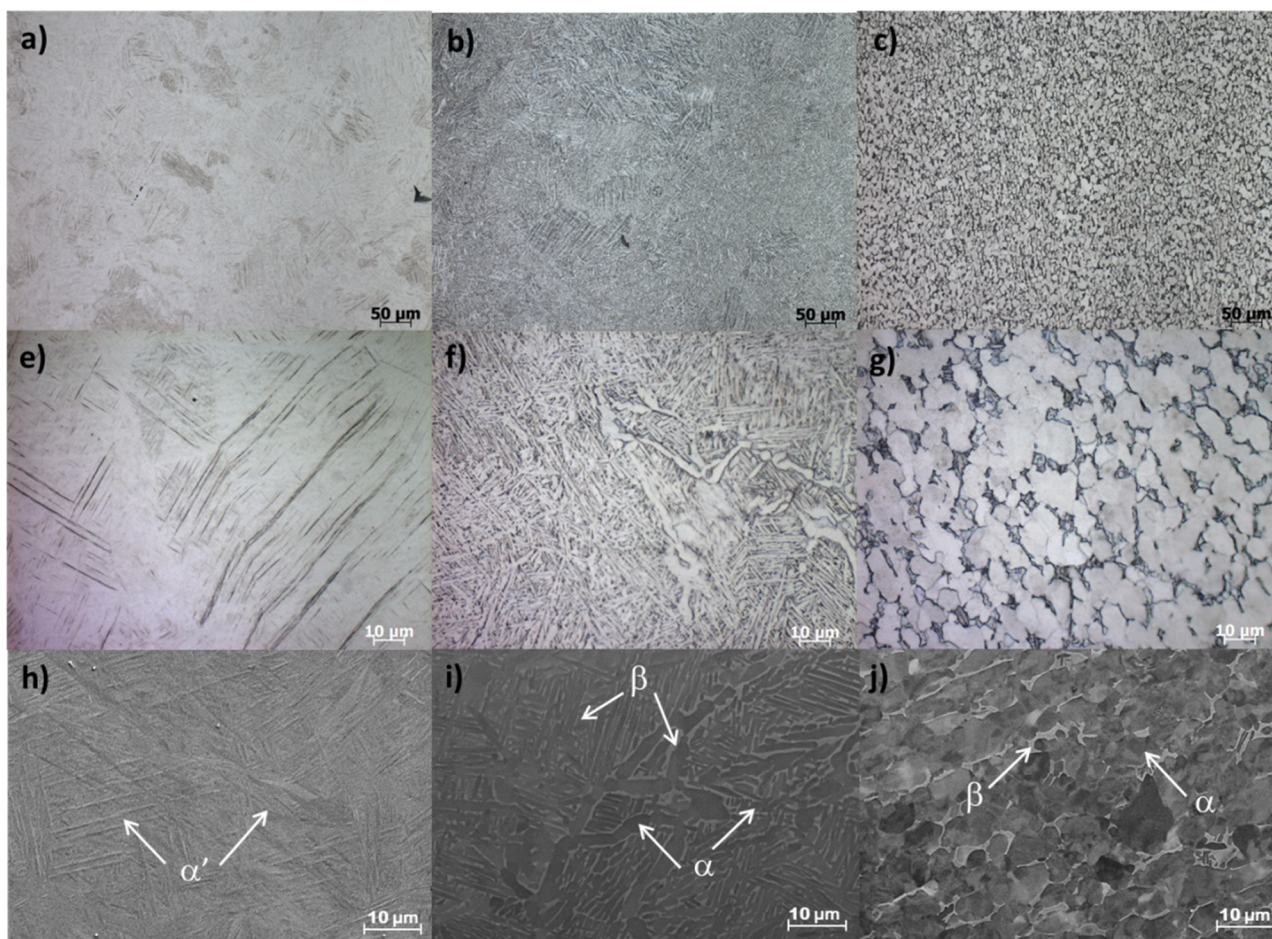


Fig. 2. Optical microscopy images of the microstructures of the a) Ti6Al4V - SLM, b) Ti6Al4V – SLM-HT and c) Ti6Al4V - WR samples at 200 × magnification and the e) Ti6Al4V - SLM, f) Ti6Al4V – SLM-HT, and g) Ti6Al4V - WR samples at 1000 × magnification, all etched with Kroll, and FE-SEM images of h) Ti6Al4V - SLM, i) Ti6Al4V – SLM-HT and j) Ti6Al4V - WR samples at 5000 × magnification in non-etched condition.

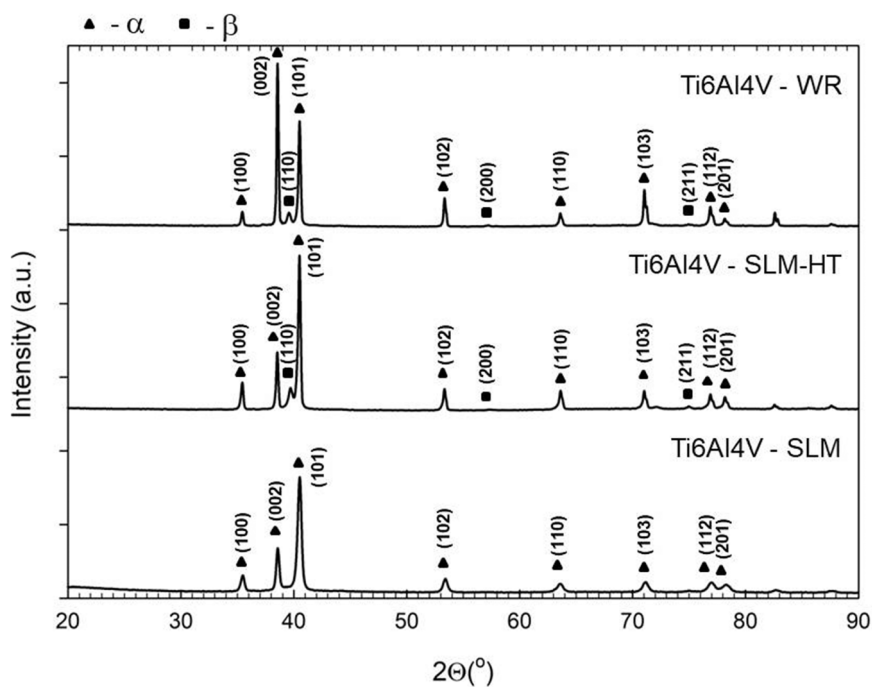
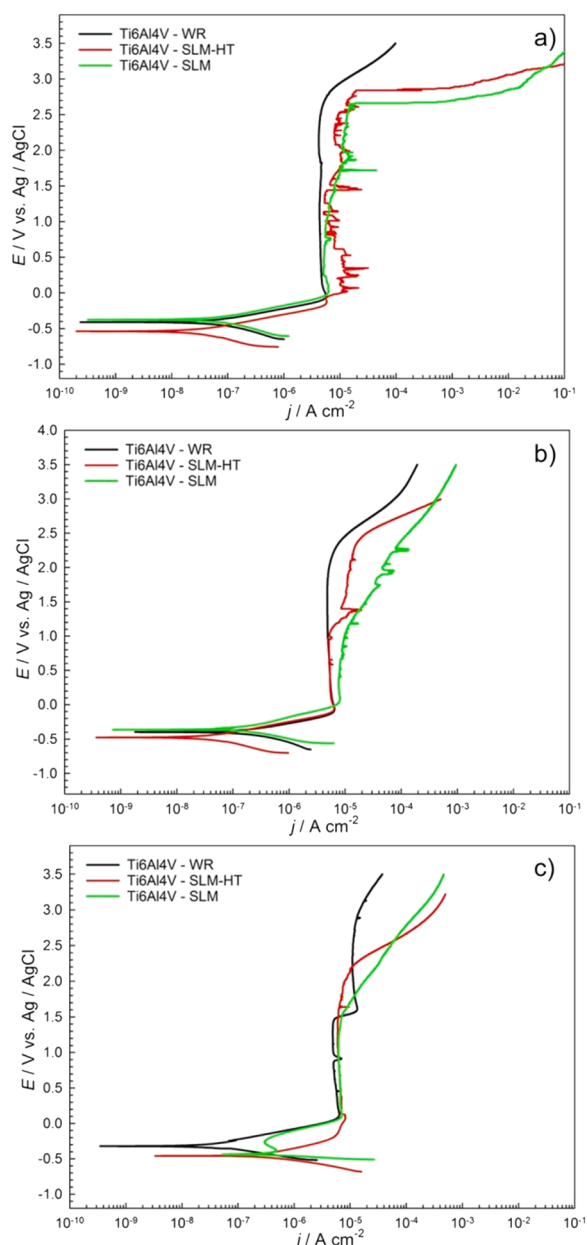


Fig. 3. XRD diffractograms of the Ti6Al4V - SLM, Ti6Al4V – SLM-HT, and Ti6Al4V - WR samples.



**Fig. 4.** PD curves for the Ti6Al4V – SLM, Ti6Al4V – SLM-HT and Ti6Al4V – WR samples measured at 37 °C in a) AS, b) AS with NaF, and c) AS with lactic acid (scan rate of 1 mV/s).

become apparent at potentials more positive than 1.5 V. In the Ti6Al4V – WR sample it remains low, while in the Ti6Al4V – SLM and Ti6Al4V – SLM-HT samples it slowly increases at more positive potentials, with less fluctuations in the current (Table 1, Fig. 4c).

PD measurements showed no significant differences between the different types of samples immersed in the various solutions. EIS was conducted in order to observe the long-term behaviour of the different Ti6Al4V samples in the various environments.

EIS spectra measured in AS, AS with NaF, and AS with lactic acid for all three types of samples (Ti6Al4V – SLM, Ti6Al4V – SLM-HT, and Ti6Al4V – WR) are presented in Fig. 5. It can be observed that EIS responses change with time.

EIS measurements for the Ti6Al4V – SLM and Ti6Al4V – SLM-HT samples in AS and EIS measurements for the Ti6Al4V – SLM sample in AS with NaF are given in Fig. 5a,b and d. For all these measurements, two time constants were observed in the high to mid frequency range.

**Table 1**

Electrochemical parameters derived from OCP, LP, and PD measurements for the Ti6Al4V samples in AS, AS with NaF, and AS with lactic acid.

		OCP		LP		PD		
		$E_{corr}$ [V]	$R_p$ [ $M\Omega$ $cm^2$ ]	$E_{corr}$ [V]	$j_{corr}$ [ $\ln A$ $cm^{-2}$ ]	$E_b$ [V]	$E_b^-$ $E_{corr}$ [V]	
AS	WR	-0.464	0.42	-0.409	64.1	2.70	3.11	
	SLM	-0.434	0.34	-0.376	83.1	2.67	3.05	
	SLM-HT	-0.546	0.65	-0.539	33.0	2.84	3.38	
AS with NaF	WR	-0.485	0.19	-0.869	183	1.52	2.39	
	SLM	-0.344	0.19	-0.364	139	1.10	1.46	
	SLM-HT	-0.477	0.45	-0.475	43.4	2.46	2.93	
AS with lactic acid	WR	-0.300	0.65	-0.320	33.3	1.46	1.78	
	SLM	-0.290	0.22	-0.440	297	1.53	1.91	
	SLM-HT	-0.442	0.17	-0.458	338	2.18	2.64	

After one week of immersion the absolute impedance at the lowest measured frequency,  $|Z|_{f=5mHz}$ , was 8.9  $M\Omega$   $cm^2$  for Ti6Al4V – SLM in AS, 5.86  $M\Omega$   $cm^2$  for Ti6Al4V – SLM-HT in AS, and 0.11  $M\Omega$   $cm^2$  for SLM in AS with NaF. For EIS responses for Ti6Al4V – WR in AS and Ti6Al4V – SLM in AS with lactic acid.

For the measurements in Fig. 5c and e only one time constant was observed, as could be observed from the Bode phase spectra; the magnitude of the impedances at the low frequency limit were 7.4  $M\Omega$   $cm^2$  for Ti6Al4V – WR in AS and 0.27  $M\Omega$   $cm^2$  for the Ti6Al4V – SLM sample in AS with lactic acid. The equivalent circuits employed to fit the EIS data are depicted in Fig. 5 and have been previously employed for Ti alloys [17,29–31].

A simple equivalent electrical circuit with one time constant was used to fit the EIS data presented in Fig. 5c and e, and an equivalent electrical circuit consisting of ( $R_1$ CPE) couple in series with electrolyte resistance was used to fit the EIS measurements in Fig. 5a, b, and d, where two time constants were observed [29].

The assumption is that oxide film that forms on a Ti-based alloy exhibits a two-layer structure, with a dense inner layer and a porous outer layer. XPS analysis (presented below) showed that the surface of the Ti6Al4V alloy (the uppermost position) is mainly composed of  $TiO_2$ ;  $Al_2O_3$  and  $V(OH)_3$  were also detected, but their surface concentrations were significantly lower.

CPE in equivalent electrical circuit stands for constant phase element and signifies the presence of a non-ideal capacitor, with varying  $n$ ,  $R_e$  represents electrolyte resistance.

$R_1$  represents barrier (inner) layer resistance, and  $CPE_1$  corresponds to the capacitance of the barrier layer.  $R_2$  corresponds to the resistance of the outer porous layer, and  $CPE_2$  corresponds to the capacitance of the outer porous layer. The values of fitted parameters, using the equivalent electrical circuits presented in Fig. 5, are given in Table S1 (Supplementary).

The values of electrolyte resistance,  $R_e$ , vary from 2 to 46  $\Omega$   $cm^2$ . High  $R_1$  was observed at all immersion times, ranging across several  $M\Omega$   $cm^2$ , showing that the oxide film on the Ti6Al4V alloy has a large resistance.  $R_2$  value, representing outer porous layer resistance, is lower. The polarization resistance ( $R_p$ ), which is the sum of the resistances  $R_1$  and  $R_2$ , is presented in Fig. 6. The highest  $R_p$  values were measured for the Ti6Al4V – WR, Ti6Al4V – SLM, and Ti6Al4V – SLM-HT samples exposed in AS, while the  $R_p$  values were lower for Ti6Al4V – SLM in AS with NaF, and Ti6Al4V – SLM in AS with lactic acid. In general, these values increase slightly with time, with the exception of the Ti6Al4V – SLM sample in AS with lactic acid (Figs. 5e and 6a).

In order to compare capacitance values for the various Ti6Al4V samples at different immersion times, C values were calculated from CPEs using the following equation [32],

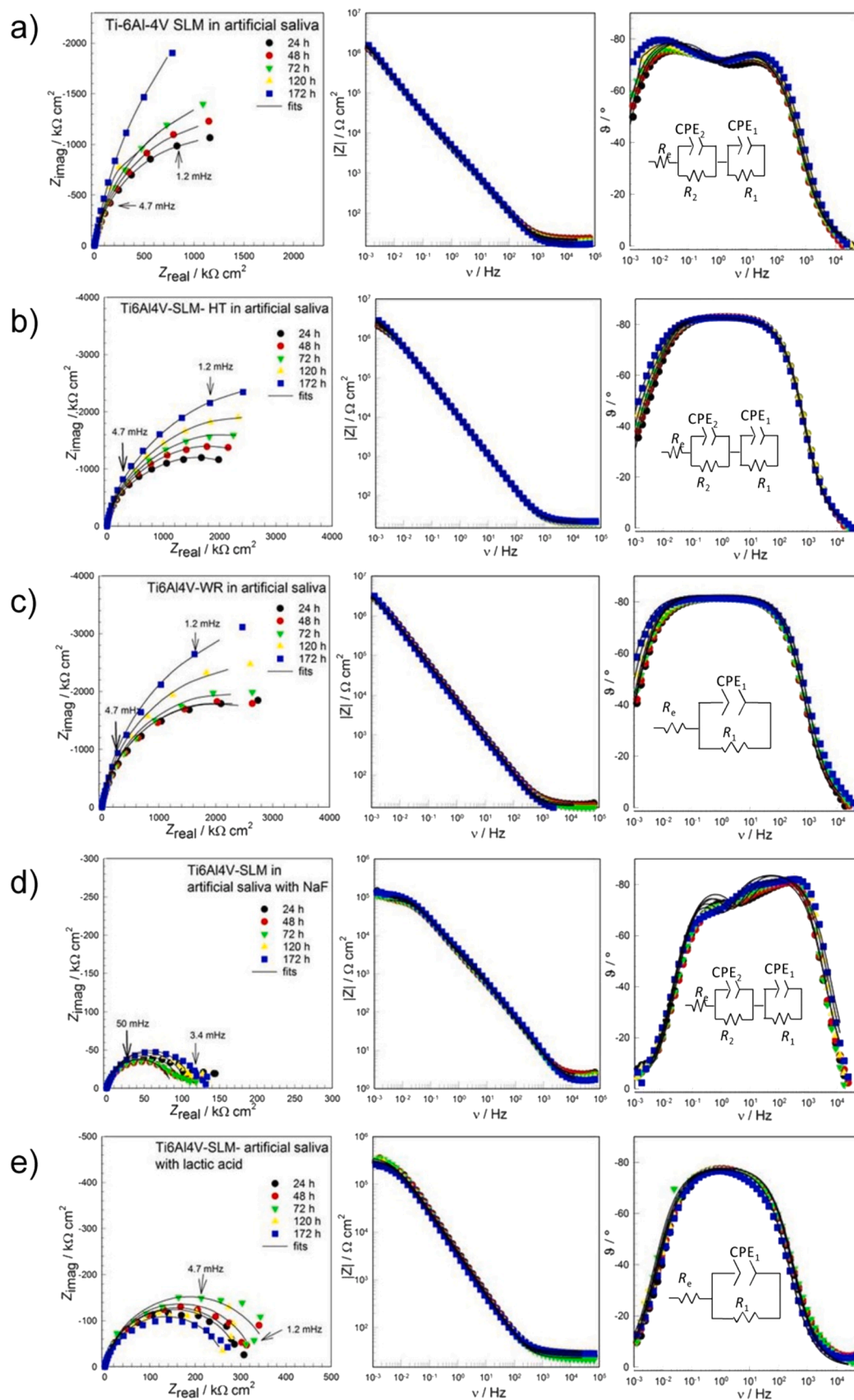
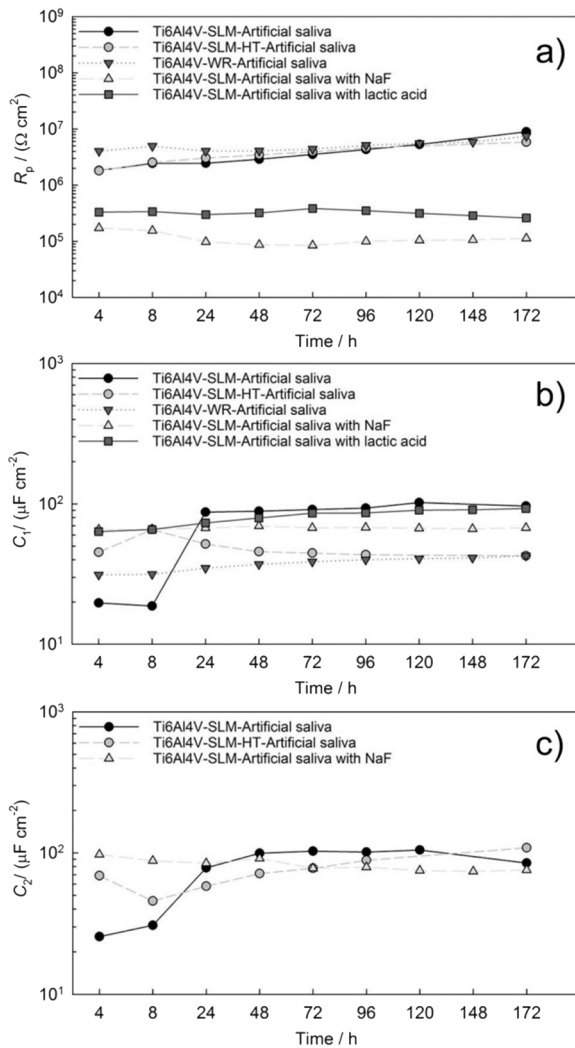


Fig. 5. Nyquist diagrams and Bode plots for the Ti6Al4V samples at various immersion times and in various environments: a) Ti6Al4V – SLM in AS, b) Ti6Al4V – SLM-HT in AS, c) Ti6Al4V – WR in AS, d) Ti6Al4V – SLM in AS with NaF, and e) Ti6Al4V – SLM in AS with lactic acid. Fitted curves are presented as solid lines.



**Fig. 6.**  $R_p$ ,  $C_1$ , and  $C_2$  values for the various Ti6Al4V samples as a function of time in the different environments at 37 °C.

$$C_x = (R_x^{1-n} \cdot CPE_x)^{1/n}, \quad (1)$$

where  $x = 1$  or 2, pertaining to  $C_1$  and  $C_2$ . Values of  $C_1$  are lower than  $C_2$  at all immersion times assessed. An increase in  $C_1$  and  $C_2$  with an increased immersion time can be attributed to a thinning of the oxide layer. A thickening of the oxide film through a decreasing  $C_2$  is observed for Ti6Al4V – SLM in AS with NaF. A similar effect has been observed previously [30]. In the case of Ti6Al4V – SLM in AS with lactic acid, the constant value of  $C_2$  and decrease in  $R_2$  (Fig. 6a) could indicate that the barrier layer either stopped growing or started to thin [30].

The thickness of the surface film,  $d$ , was evaluated using the Eq. (2).

$$d = \frac{\varepsilon \cdot \varepsilon_0 \cdot A}{C_1}, \quad (2)$$

where  $\varepsilon$  is the dielectric constant,  $\varepsilon_0$  is vacuum permittivity ( $8.85 \cdot 10^{-14}$  F/cm), and  $A$  is the surface area, in  $\text{cm}^2$ . Based on Eq. 2, the constant value of capacitance indicates a constant thickness of the passive layer. The thickness of the barrier layer from capacitance values  $C_1$  was calculated, using 100 for a value of dielectric constant for  $\text{TiO}_2$  [33].

The calculated thicknesses were 0.9 nm for Ti6Al4V – SLM in AS and in AS with lactic acid, 2.0 nm for Ti6Al4V – SLM-HT and Ti6Al4V – WR in AS, and 1.3 nm for Ti6Al4V – SLM in AS with NaF.

### 3.3. Immersion test

Results of the ion release tests are presented in Figs. 7 and 8. The amounts released on each sampling day are plotted as the cumulative values of metal ions released per  $\text{cm}^2$  including that day. The total amounts of Ti and Al ions increased at a faster rate at the beginning of exposure (up to day 7), compared to later on, in all three testing environments.

The lowest release of Ti and V ions in AS was measured in the Ti6Al4V – WR sample, and the highest in Ti6Al4V – SLM. The opposite was observed with respect to the release of Al ions in AS i.e the highest amounts were measured in Ti6Al4V – WR and the lowest in Ti6Al4V – SLM. In AS with NaF the amounts of the three elements followed the same order; the lowest amount of ions were released from Ti6Al4V – SLM and the highest from Ti6Al4V – SLM-HT. In AS with lactic acid, no significant difference was observed in the amounts of Ti and V ions released. In the case of Al, higher amounts were released in Ti6Al4V – SLM-HT.

Fig. 8 presents the total amounts of ions released, and the sum of all ions released over 42 days of exposure.

The total ion release after 42 days of exposure was the lowest in the Ti6Al4V – SLM samples exposed to AS (below  $1 \mu\text{g}/\text{cm}^2$ ). Exposure to AS with NaF led to a total release of approximately  $5 \mu\text{g}/\text{cm}^2$  of measured metal ions, while the highest amounts were measured following exposure to AS with lactic acid, where values of up to approximately  $60 \mu\text{g}/\text{cm}^2$  were observed in the Ti6Al4V – SLM sample. Overall, the lowest total amount of ions released was observed in the Ti6Al4V – SLM sample exposed to AS.

In AS, the ion released in the highest amounts (in terms of the total amount of all three ions measured, relative to the area of the sample) was Al (60%, 73% and 83% for the Ti6Al4V – SLM, Ti6Al4V – SLM-HT and Ti6Al4V – WR samples, respectively). This was followed by Ti (32%, 22% and 14% in the Ti6Al4V – SLM, Ti6Al4V – SLM-HT and Ti6Al4V – WR samples, respectively) and, in the lowest amount, V ions (8%, 5% and 3%, for the Ti6Al4V – SLM, Ti6Al4V – SLM-HT and Ti6Al4V – WR samples, respectively).

In AS with NaF, a lower amount of ions were released from Ti6Al4V – SLM than from the Ti6Al4V – SLM-HT sample. In AS with lactic acid, the total amount of ions released was measured to be slightly lower in Ti6Al4V – SLM-HT than in the Ti6Al4V – SLM sample. In AS with NaF, and the AS with lactic acid, Ti ions were released in a higher amount than the V and Al ions. More Al ions (regarding to the total amount of all measured released ions) were released in AS with lactic acid than in AS with NaF (see Fig. 8b and c). In both AS with NaF and AS with lactic acid, Ti ions were released in the highest amount (around 90% in AS with NaF and between 77% and 84% in AS with lactic acid). In AS with NaF, more V ions (approx. 7%) were released than Al ions (approx. 2%). The proportions of Al and V in AS with lactic acid were the opposite, with a higher amount of Al ions (between 12% and 18%) being released than V ions (approx. 3%).

### 3.4. XPS measurements

XPS analysis showed that, before the Ar-ion sputtering process, the Ti6Al4V – SLM samples immersed in each of the three solutions displayed Ti, Al, V, C, and O signals. The Ti6Al4V – SLM sample immersed in AS with NaF also showed a signal for F. Atomic surface concentrations were calculated based on the high-resolution signals and are summarized in Table 2. Fitting of the Ti 2p spectra was performed based on the recommendation of Biesinger et al. [34] and can be seen in Fig. 9.

Next, XPS depth profiling was performed to investigate the structure of the passive oxide film formed on the Ti6Al4V – SLM samples immersed in the three different solutions i.e. AS, AS with NaF, and AS acidified with lactic acid.

Previous XPS depth profiling studies on Ti6Al4V have focused on the analysis of the passive film build-up at different applied anodic

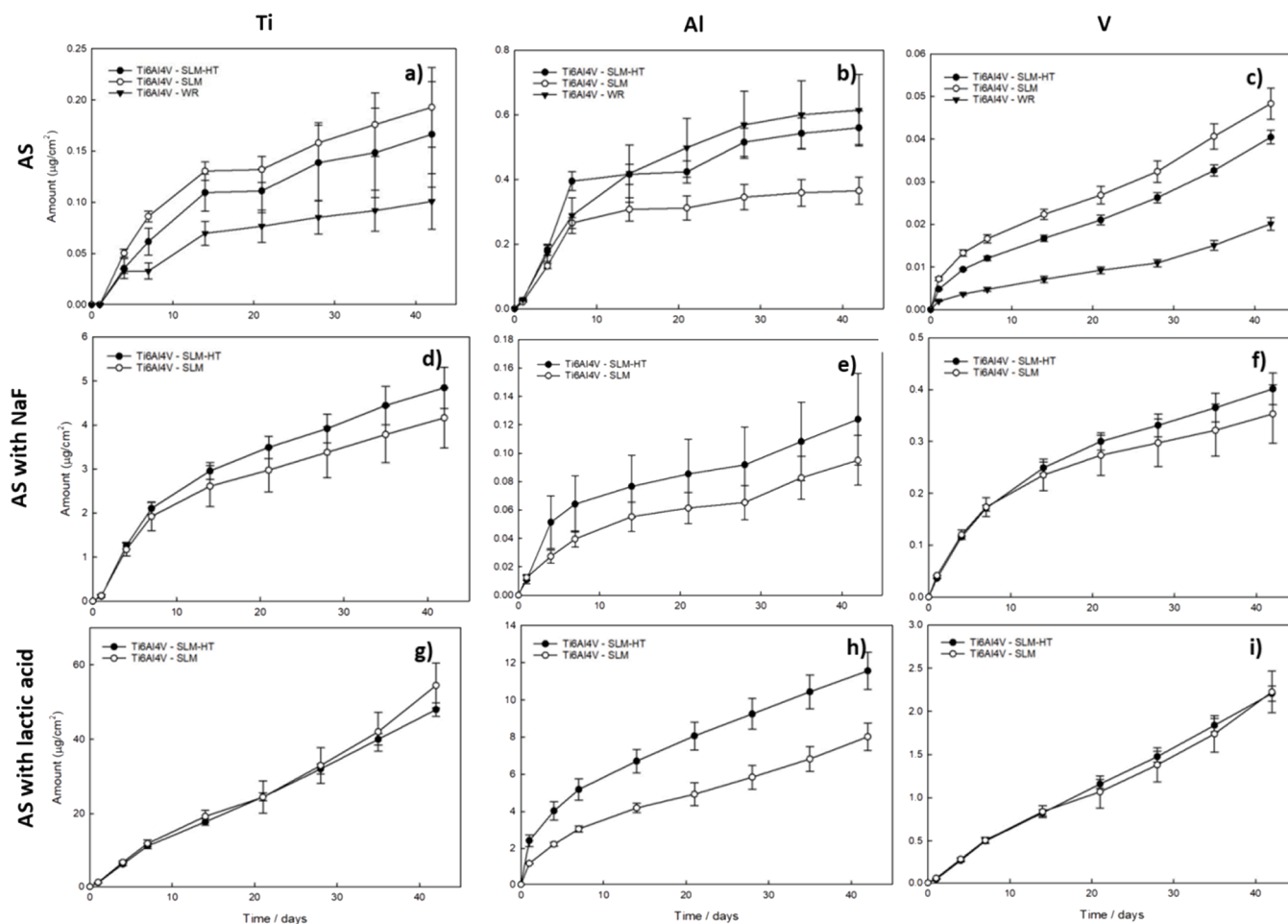


Fig. 7. Amounts of Ti, Al, and V ions measured during the immersion tests.

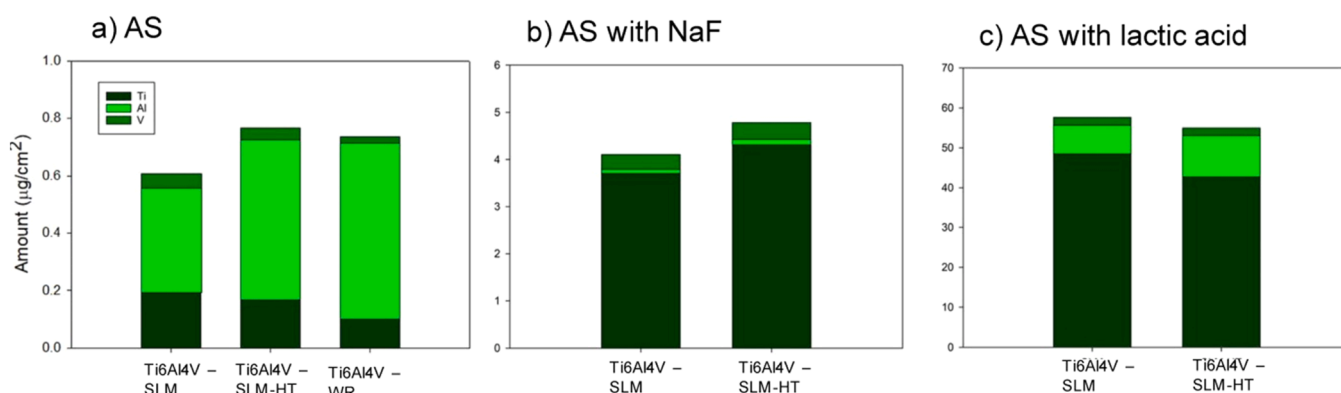


Fig. 8. Total amounts of Ti, Al, and V released over 42 days of exposure in a) AS, b) AS with NaF, and c) AS with lactic acid.

potentials in a body fluid solution [17]. Recently, SLM, EBM (electron beam melting), and cast samples of Ti6Al4V alloy were compared in order to determine any differences in the surface film [35]. It was found that SLM printed samples in as printed condition contained more titanium oxides than EBM and cast samples, with TiO<sub>2</sub> being the major constituent of oxides in the surface film. Moreover, the oxide film on the SLM sample was thinner than that on the EBM sample. Furthermore, XPS analysis of the SLM printed Ti6Al4V samples, formed using a laser energy density of 39 J/mm<sup>3</sup>, showed that TiO<sub>2</sub> was the major component on the surface, while no V-containing species were detected on the surface prior to sputtering [24]. The latter does not necessarily mean

that V-containing species were not present on the surface, however, as the detection limit of the XPS device used might have been too high to detect the V 2p signal on the surface.

Fig. 10a, Figs. 11a and 12a show the respective Ti 2p spectra for Ti6Al4V - SLM samples immersed in AS, AS with NaF, and AS with lactic acid for 7 days. The Ti 2p spectra include three features prior to sputtering, as denoted by the positions of the dashed lines marked 1, 2, and 3 (the lowest spectra in Fig. 10a, Figs. 11a and 12a). All three surfaces were rich in TiO<sub>2</sub>, as confirmed by the most intense peak at dashed line 2 ( $BE = 458.4$  eV), which corresponds to Ti 2p<sub>3/2</sub> for Ti(IV), while the peak at the position of dashed line 1 ( $BE = 464.2$  eV) corresponds to Ti

**Table 2**

Atomic surface concentrations determined based on XPS high-resolution spectra measurements (conducted before the sputtering process). The amount of Ti species was determined based on the fitted data given in Fig. 9.

	Ti [at%]	Al [at %]	V [at%]	C [at%]	O [at %]	F [at %]
AS	25.8	3.6	0.5	16.1	54.0	–
AS with NaF	18.6	2.9	0.5	25.1	52.4	0.5
AS with lactic acid	17.9	3.1	0.6	29.0	49.4	–
	Ti(0) [%]	Ti(II) [%]	Ti(III) [%]	Ti(IV) [%]		
AS	8.9	6.4	8.3	76.3		
AS with NaF	9.0	6.4	8.2	76.4		
AS with lactic acid	13.5	9.8	12.0	64.7		

$2p_{1/2}$  (for Ti(IV)) [36]. A less intense peak at the position of dashed line 3 ( $BE = 453.8$  eV) corresponds to Ti  $2p_{3/2}$  for the metal Ti (Ti(0)). On the other hand, Ar ion sputtering can affect the unwanted reduction in Ti. Although one might assume that the peaks corresponding to Ti(III) and Ti(II) species are present on the surface during sputtering (the  $BE$  region for Ti  $2p_{3/2}$  between the dashed lines 2 and 3 in Fig. 10a, Figs. 11a and 12a), they may also be a result of the sputtering process, and are not necessarily present in the passive oxide layer, making interpretation of the Ti species less certain for the spectra acquired during sputtering.

Fig. 10b, Figs. 11b and 12b show the high-resolution spectra for the Al 2p measured before and after sputtering for a given time (the sputtering time is indicated for each spectrum). The most intense feature at dashed line 1 corresponds to  $Al_2O_3$ , while the feature at dashed line 2 corresponds to metallic Al. Ar ion sputtering of the samples resulted in a less intense peak for  $Al_2O_3$ , and a more intense peak for metallic Al. The  $Al_2O_3$  peak disappears after 1095 s of sputtering in Figs. 10b and 12b, while it disappears after 1695 s of sputtering in Fig. 11b. The latter might indicate that the layer containing  $Al_2O_3$  in the Ti6Al4V - SLM sample immersed in AS with NaF is thicker than the surface layer formed in the Ti6Al4V - SLM samples immersed in the other two solutions.

Fig. 10c, Figs. 11c and 12c show the high-resolution spectra for the V 2p measured before and after sputtering for a given time (as labelled in the spectra). A feature at dashed line 2 ( $BE = 514.1$  eV for V  $2p_{3/2}$ ), which was the most intense in the V 2p spectra before sputtering, corresponds to  $V(OH)_3$  [34] and probably also some  $V_2O_5$  underneath (as

this peak is relatively broad). After the first sputtering cycle, the shape of the spectra changed, in that the feature representing  $V(OH)_3$  becomes less intense, and then disappears altogether after a few sputtering cycles (spectral feature positioned at dashed line 2), while the features at dashed lines 1 ( $BE = 511.9$  eV) and 3 ( $BE = 519.6$  eV) become more intense. The features at dashed lines 1 and 3 correspond to metallic V. During depth profiling with Ar ion sputtering, the X-ray beam may affect V speciation, making the analysis of V during depth profiling less reliable [34].

Based on the results given above, it can be concluded that the surface layers of all three samples comprised  $TiO_2$ ,  $Al_2O_3$ , and  $V(OH)_3$  prior to sputtering. As the sputtering time increased these species were gradually removed, and more corresponding metallic species were obtained. The depth profiles for the three samples are shown in Fig. 10d, Figs. 11d and 12d. The initial sputtering with 5 keV  $Ar^+$  should remove all adventitious carbonaceous species, but the presence of C signals persisted in all the samples, being measured until the end of the sputtering process (the C 1 s signal disappears only in the middle of the sputtering process in Fig. 11d, but again becomes intense at the end of the sputtering process). The presence of C and O signals can be explained by 2 effects, namely, the adsorption of residues from the vacuum and a shadowing effect. The presence of the C signal during depth profiling (after the removal of adventitious carbonaceous species), and the O signal after the removal of the Ti, Al, and V oxides (after sputtering for 1095 and 1695 s, as explained above), could be due to the adsorption of C- and O- containing species from the residual vacuum atmosphere onto the reactive surface of the SLM, primarily consisting of Ti, which is highly reactive and newly forms after each sputtering cycle. A second reason for the presence of C and O signals is the shadowing effect, which occurs due to the incomplete and non-uniform removal of these species from the surface during sputtering.

### 3.5. AFM measurements

All Ti6Al4V - SLM samples were prepared using the same procedure as the metallographic samples (as described in Section 2.2.) in order to achieve a mirror-like surface. The samples were then exposed to AS, AS with NaF, and AS with lactic acid for 1 week at 37 °C. The AFM images are shown in Fig. 13. Mean surface nano roughness ( $S_a$ ) values were used to estimate the corrosion-induced damage. The lowest  $S_a$  ( $0.220 \pm 0.048$  nm) was determined in the sample immersed in AS, while the

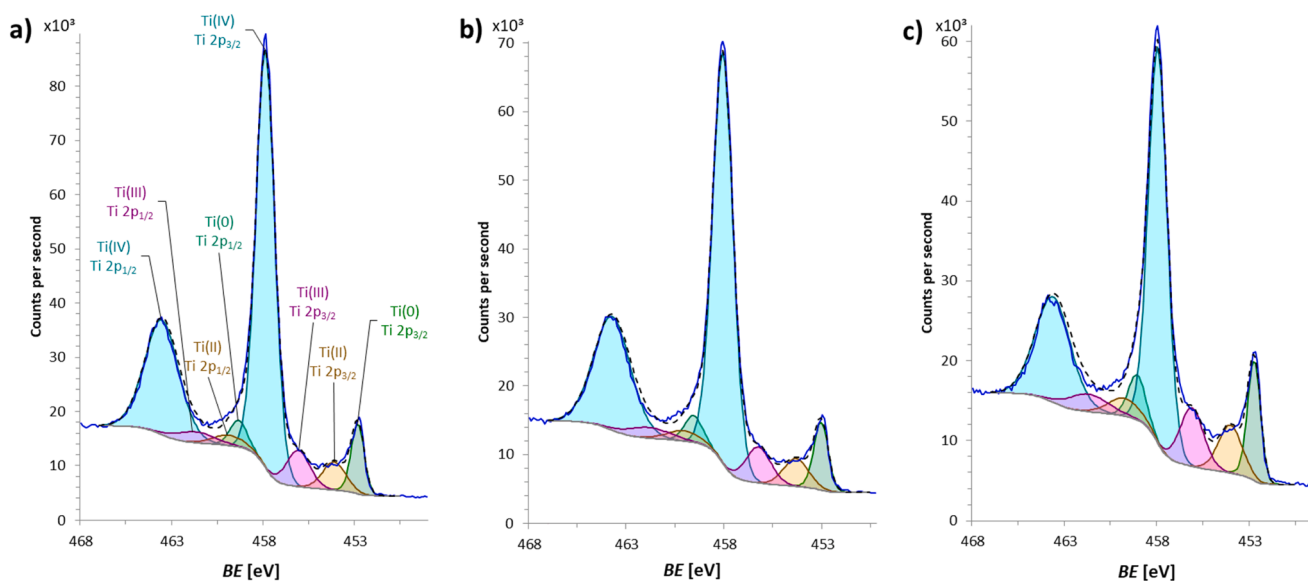


**Fig. 9.** Ti 2p fitted data for the spectra, acquired before sputtering, for the Ti6Al4V - SLM sample immersed for 7 days in a) AS, b) AS with NaF, and c) AS with lactic acid. The solid and dashed lines represent the measured and fitted spectra, respectively.

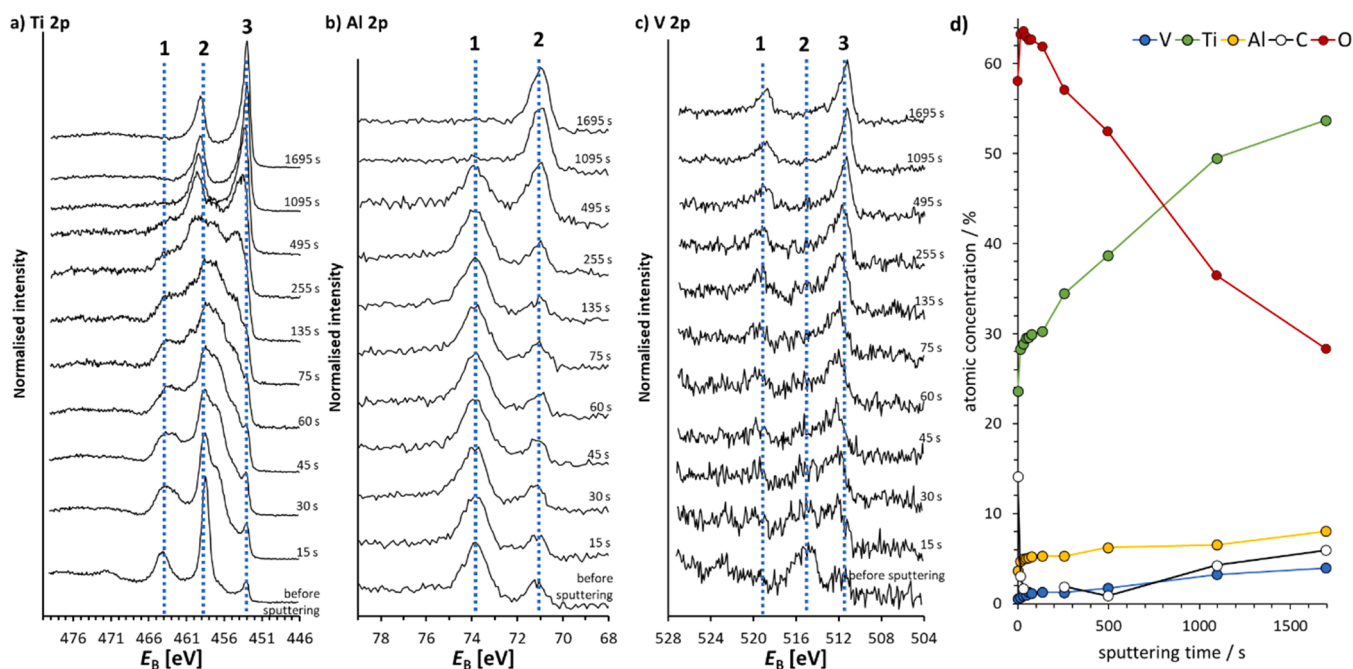


Fig. 10. High-resolution XPS spectra for Ti6Al4V - SLM immersed in AS for 7 days; a) Ti 2p, b) Al 2p, and c) V 2p before and after sputtering with 5 keV Ar<sup>+</sup>, and d) the corresponding XPS depth profile.

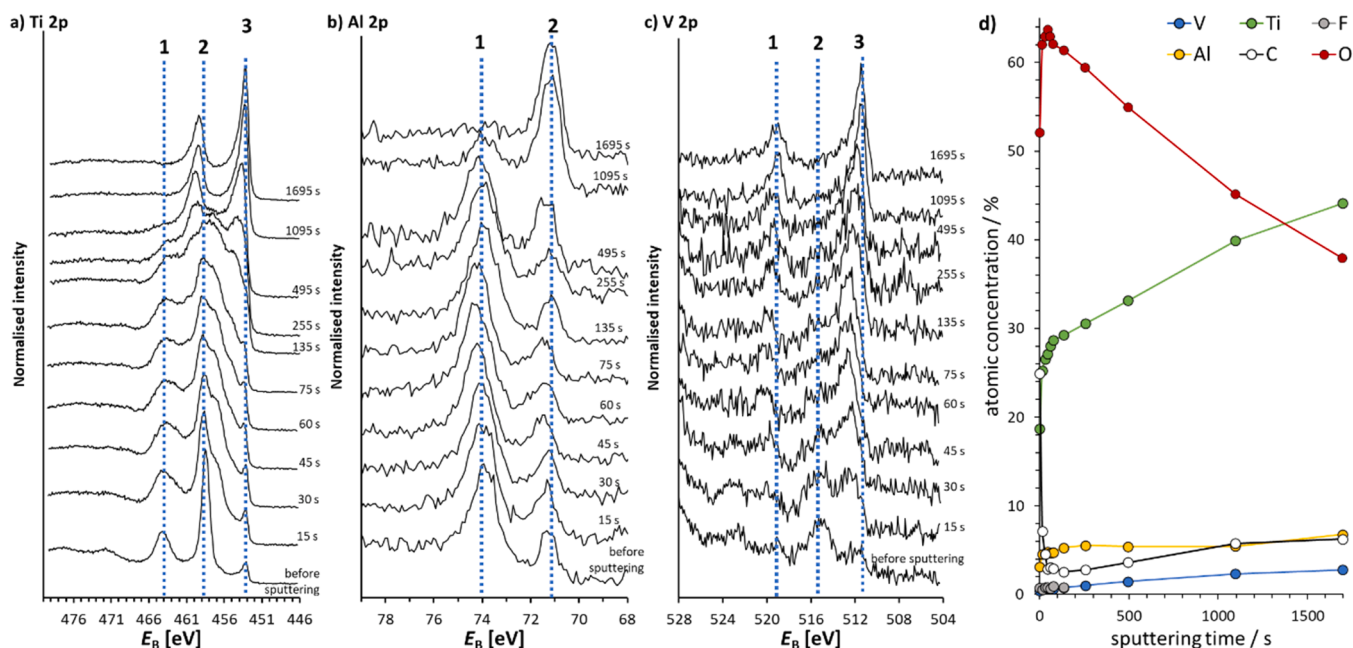


Fig. 11. High-resolution XPS spectra for Ti6Al4V - SLM immersed in AS with NaF for 7 days; a) Ti 2p, b) Al 2p, and c) V 2p before and after sputtering with 5 keV Ar<sup>+</sup>, and d) the corresponding XPS depth profile.

sample immersed in AS with NaF was rougher ( $S_a = 0.367 \pm 0.063$  nm). The  $S_a$  value was highest in AS with lactic acid (at  $0.440 \pm 0.086$  nm), in which the highest ion release was also measured, as presented below.

### 3.6. ToF-SIMS measurements

Fig. 14 shows an RGB (red, green, blue) overlay of 2D images for Ti<sup>+</sup>, Al<sup>+</sup>, and V<sup>+</sup>, respectively representing the distribution of Ti-, Al-, and V-containing species on the surface of each of the three samples [37,38]. These species may originate from the metals and, to a greater extent,

from their metal oxides. All three surfaces show a homogeneous distribution of all three species across the surface.

Next, 3D distribution analysis was performed in both positive and negative polarity. A new surface area was analyzed for each polarity. It is claimed that the M<sup>+</sup> signals are used to compensate for the matrix effects, where M represents the metals, i.e. Ti, Al, and V in the present study. On this basis, the CsTi<sup>+</sup>, CsAl<sup>+</sup>, and CsV<sup>+</sup> peaks were used for 3D imaging (Fig. 15a). On the other hand, the Cs<sup>+</sup> sputter beam enhances the production of negative ions. Ions representing metal oxides, i.e. TiO<sup>-</sup>, AlO<sup>-</sup>, and VO<sup>-</sup> for Ti-, Al-, and V-oxide, respectively [38–40], were

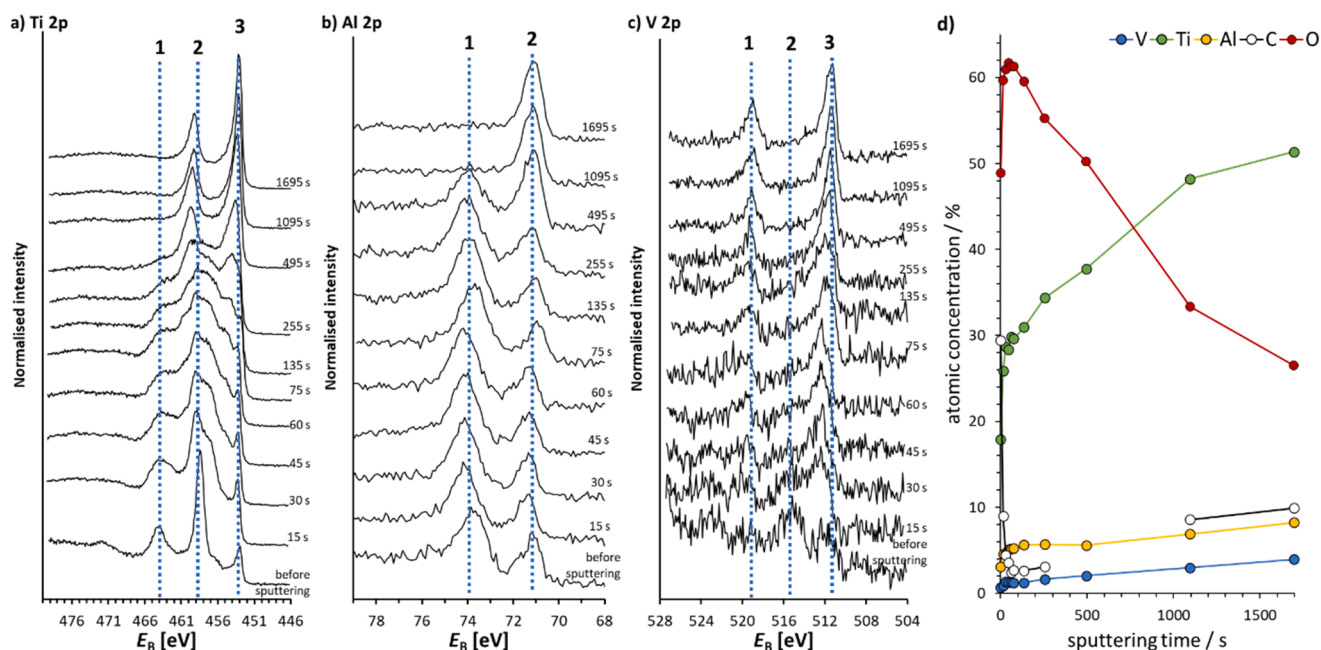


Fig. 12. High-resolution XPS spectra for Ti6Al4V - SLM immersed in AS with lactic acid for 7 days; a) Ti 2p, b) Al 2p, and c) V 2p before and after sputtering with 5 keV Ar<sup>+</sup>, and d) the corresponding XPS depth profile.

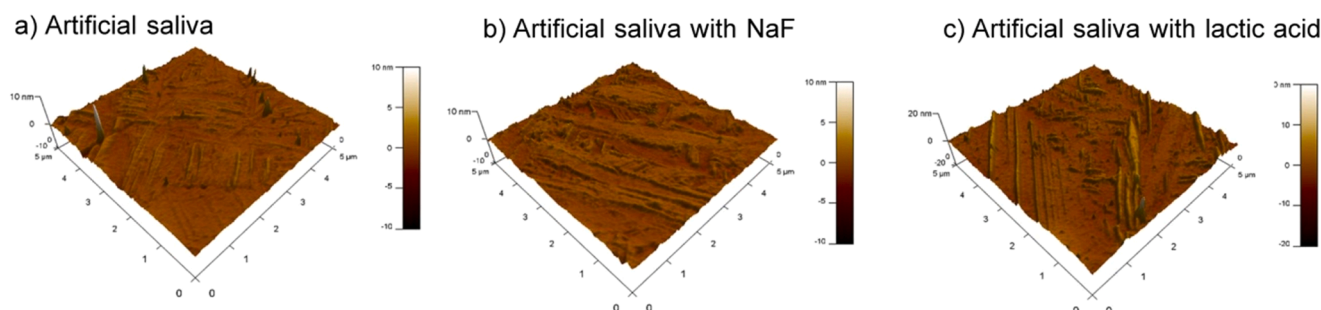


Fig. 13. AFM images for the Ti6Al4V - SLM samples after 1 week of exposure to a) AS, b) AS with NaF and c) AS with lactic acid.

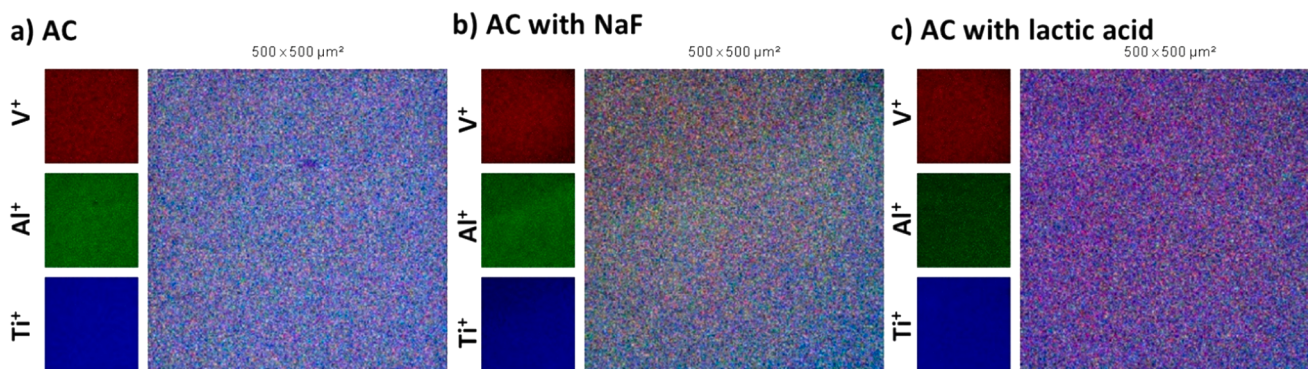


Fig. 14. 2D ToF-SIMS imaging of Ti-, Al-, and V-containing species on the surfaces of samples exposed to a) AS, b) AS with NaF, and c) AS with lactic acid.

therefore used to determine the spatial distribution of oxides / hydroxides on the surface of the samples. Additionally, the signals for Ti<sup>+</sup>, Al<sup>+</sup>, and V<sup>+</sup> were respectively used to characterize the distribution of Ti-, Al-, and V-containing species (metals and their corresponding oxides). The distribution of F<sup>-</sup> was also considered for the sample immersed in AS with NaF (as shown in Fig. 15b).

As expected, the signals representing metal oxides are in the

uppermost position (Fig. 15b). A closer look at Fig. 15b shows that the position at the very top primarily consists of Al<sub>2</sub>O<sub>3</sub> and TiO<sub>2</sub> (as also determined by the XPS measurements). The surfaces were especially rich in Al<sub>2</sub>O<sub>3</sub> (as seen by the overlay images in Fig. 15a). Moreover, V<sub>2</sub>O<sub>3</sub> is located a few atomic monolayers below the Al<sub>2</sub>O<sub>3</sub> and TiO<sub>2</sub>, whereas the uppermost position is composed of V(OH)<sub>3</sub> (as shown above from the XPS analysis). On the other hand, the sample immersed in AS with NaF

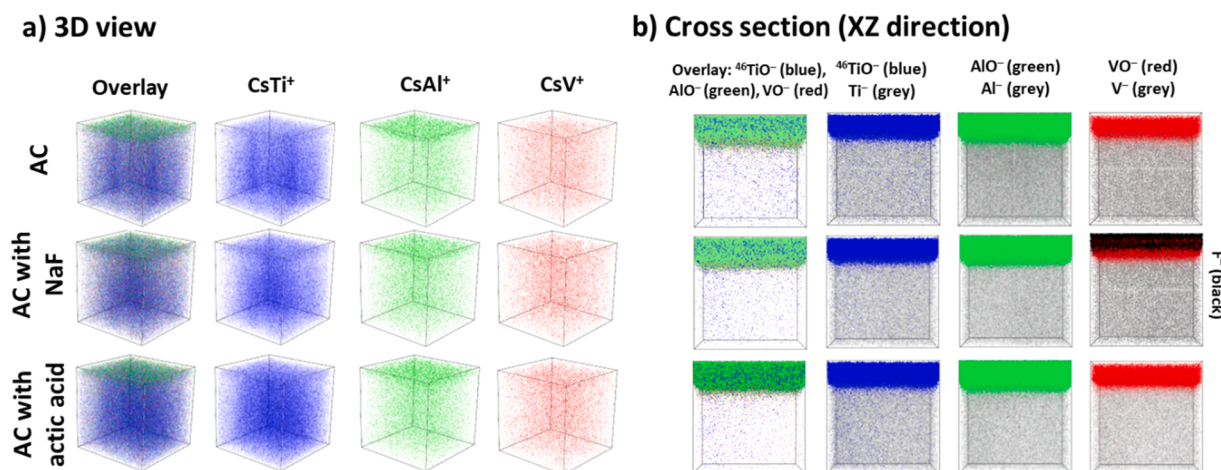


Fig. 15. ToF-SIMS 3D imaging in a) positive and b) negative polarity. Sputtering was performed using a 500 keV  $\text{Cs}^+$  sputter beam over an area of 300 by 300  $\mu\text{m}$ , with an analysis spot size of 100 by 100  $\mu\text{m}$ .

also shows a signal for  $\text{F}^-$ , which, in this case, was positioned on top of the oxide layer (Fig. 15b). After sputtering off the metal oxides, the bulk material, made of Ti, Al, and V, is very homogeneous (Fig. 15a and b).

#### 4. Discussion

Ion release tests were conducted according to a newly released standard for testing prosthodontic materials, ISO 10271:2020-Dentistry — Corrosion test methods for metallic materials. Since samples produced by additive manufacturing are presently being explored, information on the release of ions in materials, produced by newly emerged technologies such as selective laser melting is very important in prosthodontics. Based on the ion release measurements of the Ti6Al4V – SLM, Ti6Al4V – SLM-HT, and Ti6Al4V – WR samples during the immersion tests, it can be concluded that the severity of the test environment increased from AS to AS with NaF, and then again to AS with lactic acid. The total amount of ions released in AS with NaF is, on average, approximately 10 times higher than that in AS, and in AS with lactic acid it is approximately 100 times higher than in AS. It should also, however, be pointed out that these amounts are still below the limits defined by the standard ISO 22674: 2016 (Dentistry – Metallic materials for fixed and removable restorations and appliances), that is 200  $\mu\text{g}/\text{cm}^2/7$  days, so the materials are therefore still deemed safe for use in dental applications.

In AS, the lowest total amount of ions was measured in the Ti6Al4V – SLM sample, while the higher amount of ions was released in the Ti6Al4V – SLM-HT and Ti6Al4V – WR samples, at levels comparable to one another (Fig. 8a). Based on martensitic  $\alpha'$  microstructure enabling more homogenous oxide development on the surface of Ti6Al4V – SLM than on  $\alpha + \beta$  microstructure of Ti6Al4V – SLM-HT and Ti6Al4V – WR, where alloying elements are unequally distributed over the surface, that would be expected [1,24,27]. The  $R_p$  values, which provide information about general (uniform) susceptibility to corrosion, were determined by EIS over 1 week of exposure confirm previous observation [27]. Also,  $R_p$  increased for the Ti6Al4V – SLM, Ti6Al4V – SLM-HT and Ti6Al4V – WR samples during 1 week of exposure, indicating the build-up of the oxide film with its protective properties (Fig. 6a). It is assumed that, in AS, the passive film remains stable over time. In a previous study, a passive film formed on Ti6Al4V in a near neutral environment was reported to consist of an inner layer (metal/oxide interface), primarily composed of  $\text{TiO}_2$  with a minor amount of suboxides  $\text{TiO}$  and  $\text{Ti}_2\text{O}_3$ , and a more porous layer, consisting of  $\text{TiO}_2$  and  $\text{Al}_2\text{O}_3$  and  $\text{V}_2\text{O}_5$ , formed at the oxide/ environment interface [1,17]. Our experiments show that Al and V oxides in the outer, porous oxide layer are less stable and also dissolve in mild environments such as AS. This can explain the fact that Al ions

were released in higher amounts than Ti and V ions, since aluminium oxide is destabilized in a slightly acidic environment [41]. In a study by Sawy et.al. [42], Al ions (163 ppb) were also released in a far higher amount than Ti ions (39 ppb) from a Ti6Al4V alloy in buffered AS following 7 days of exposure. The amount of Al released from a Ti6Al4V alloy in a near-neutral buffered 0.15 M NaCl solution was also reported by Milošev et. al. to be a few times higher than the release of Ti [42,43]. On the other hand, in our study the amount of V ions released was low. The XPS depth profile measurement showed that the V detected at the top of the outermost oxide layer was in the form of  $\text{V}(\text{OH})_{3-}$ . Significantly different electrochemical responses of the Ti6Al4V – SLM-HT, Ti6Al4V – WR, and Ti6Al4V – SLM samples were observed from the PD measurements. A comparison of the PD curves shows the current density in the anodic region, with frequent current fluctuations occurring in the Ti6Al4V – SLM-HT sample, and to some extent for TiAlV-SLM sample. Following 1 week of exposure to AS, similar  $R_p$  values, as determined by EIS, were measured for all the samples (Fig. 6).

In AS with NaF, the lowest total ion release was measured in the Ti6Al4V – SLM samples. Ti ions in this environment were released in the highest amount, while the amount of V ions released was higher than Al, which is consistent with the research presented by Milošev et. al. [43]. Fluoride ions in AS interact with hydrogen ions, forming a slightly acidic local environment [16], which is detrimental for the passive layer due to the dissolution of  $\text{TiO}_2$ . In the Ti6Al4V – SLM samples, the  $R_p$  values determined in AS with NaF were lower than those measured in AS alone (Fig. 6a). The constant capacitance values of the passive film, together with the low  $R_p$  value, suggest a reduction in the barrier properties takes place at the same time as an increase in dissolution. Based on results of the immersion test in AS with NaF, however, it can be concluded that  $\text{V}(\text{OH})_3$  is attacked more severely than  $\text{Al}_2\text{O}_3$ . Based on Pourbaix diagrams [41] for Al and V oxides, they dissolve at pH values below 3 and 5.5, respectively. It might therefore be assumed that the local pH drop arising from the formation of HF in AS with added NaF is less favorable for the stability of V-hydroxide than it is for Al-oxide. Results of the PD measurements are very similar to those in AS, with the exception that values of passive current density shifted towards slightly higher values at potentials above 1.0 V (Fig. 4a), showing the lower homogeneity of the passive layer.

In the most aggressive environment, AS with lactic acid, the  $R_p$  values for the Ti6Al4V – SLM sample were low as deduced from EIS and also for SLM materials, as deduced by  $R_p$  measurements (Table 1). The passive film probably underwent dissolution, as was also observed from the capacitance values,  $C_1$ , of the passive film (Fig. 5).

The total amount of ions released from the Ti6Al4V – SLM and Ti6Al4V – SLM-HT samples is the highest in AS with added lactic acid,

with similar values occurring in each (Fig. 7c). Here, the elemental composition of the ions released reflects the chemical composition of the alloy: around 80% of all ions released are Ti ions, with 12% (Ti6Al4V - SLM) to 19% (Ti6Al4V - SLM-HT) Al ions and approximately 3.5% V ions. The higher percentage of Al ions released with respect to the amount of Al in the alloy could be due to the higher amount of aluminium oxide in the outer passive layer, but it should also be pointed out that Al is an  $\alpha$ -phase stabilizer. This could be an indicator of preferential corrosion of this phase regarding to  $\beta$ -phase in acidic solutions, [1] which could occur under the specific condition of a freely corroding system (no applied potential) [9]. A lower corrosion resistance of the lamellar  $\alpha + \beta$  Ti6Al4V - SLM-HT compared to martensitic  $\alpha'$ , as contained in Ti6Al4V - SLM, has also been reported in the literature [1].

Based on above mentioned findings, the mechanism of oxide film destabilization during exposure in AS, AS with NaF, and AS with lactic acid is proposed in Fig. 16. The structure of the passive film and underlying surface of Ti6Al4V alloy was schematically presented employing results of XPS, AFM, ToF-SIMS, EIS, and ion release measurements.

The mechanism proposed in Fig. 16 consists of two main processes for Ti6Al4V - SLM:

The intensity of dissolution and its effect on roughness is denoted as a dashed line, where active corrosion (dissolution), is presented based on the results of AFM measurements and ion migration test. Namely, almost 10-times more intensive dissolution took place in AS with NaF, while in AS with lactic acid, approximately 100-times higher ion release was determined, which is supported by the findings reported previously [44, 45].

In the proposed mechanism, AS is a reference environment to which the effect of the other two environments is compared. In AS with NaF, the slightly thicker oxide film is observed, most likely due to outer - porous part; on the other hand,  $R_p$  of this oxide is lower than in AS, most likely because of detrimental action of  $F^-$  incorporated in this part of the oxide layer. Similar was reported previously [45].

In AS with lactic acid, the thickness of the oxide layer is similar to that of the oxide layer formed in AS, according to ToF-SIMS, XPS and EIS measurements. However, corrosion resistance (evaluated based on  $R_p$  values) is significantly lower for AS with lactic acid compared with AS. Moreover, AFM measurements indicate higher surface roughness for the AS with lactic acid compared with AS pointing at active dissolution observed by higher ion release, as also shown previously [16].

## 5. Conclusions

This study presents microstructural, electrochemical, topographic, and spectroscopic analysis of Ti6Al4V samples prepared by SLM and. Ti6Al4V samples were produced both with and without heat treatment and compared to the same alloy produced by the conventional wrought process. The samples were immersed in artificial saliva, artificial saliva with added NaF, and acidified artificial saliva (containing lactic acid) simulating inflammatory conditions.

The main findings of this research are:

- 1) From electrochemical measurements it could be observed that passive layer developed on the SLM produced Ti6Al4V alloy exposed to artificial saliva with lactic acid was less protective (stable) than in artificial saliva and artificial saliva with NaF.
- 2) Results from the ion release study showed that the highest amount of the measured Ti, Al, V ions was released in artificial saliva with lactic acid, which was approximately 100 times higher than in artificial saliva alone. The measured amounts were still, however, below the allowable limits for total ion release in alloys used for dental applications.
- 3) Complementary surface analysis using XPS, AFM, and ToF-SIMS offered detailed insight into the passive layer on SLM fabricated Ti6Al4V in different environments by defining the spatial distribution of certain species.
- 4) Much higher intensity of the corrosion process taking place on Ti6Al4V alloy arises from the chemistry of the environment than from the alloy microstructure, which is defined by the type of manufacturing process of the alloy. However, from the results of the ion release study, higher corrosion resistance was proven for SLM fabricated Ti6Al4V alloy consisting of  $\alpha'$  martensitic microstructure compared to heat treated SLM and wrought alloys with  $\alpha + \beta$  microstructure.

## CRedit authorship contribution statement

**M. Bajt Leban:** Investigation, Conceptualization, Formal analysis, Writing - original draft, Writing - review & editing. **T. Kosec:** Writing - review & editing, Formal analysis, Validation, Supervision, Funding acquisition. **M. Finsgar:** Formal analysis, Writing - review & editing.

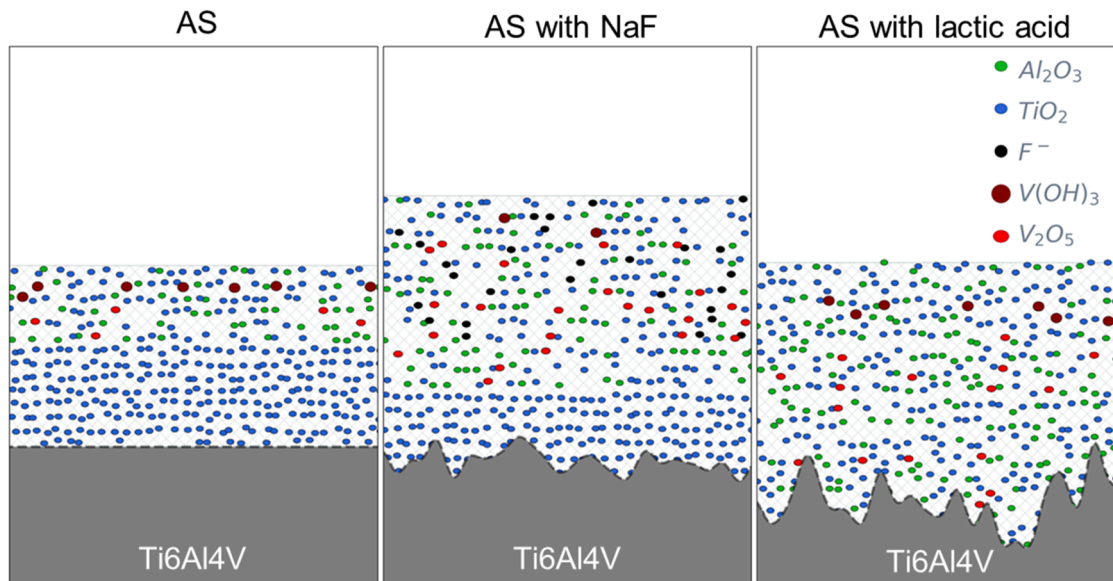


**Fig. 16.** Tentative mechanism of oxide destabilization of Ti6Al4V alloy exposed to a) AS, b) AS with NaF, and c) AS with lactic acid. Ion release results show increased release in AC with lactic acid and AS with NaF compared to AS.

## Declaration of Competing Interest

The authors declare that they have no known competing financial interests or personal relationships that could have appeared to influence the work reported in this paper.

## Data Availability

Data will be made available on request.

## Acknowledgments

The authors acknowledge financial support from the Slovenian Research Agency (Grant Nos. L2-1831, P2-0273, J1-2470, and P2-0118). The project is co-financed by the Republic of Slovenia, the Ministry of Education, Science and Sport, and the European Union through the European Regional Development Fund.

## Appendix A. Supporting information

Supplementary data associated with this article can be found in the online version at [doi:10.1016/j.corsci.2022.110716](https://doi.org/10.1016/j.corsci.2022.110716).

## References

- [1] P. Bocchetta, L.-Y. Chen, J.D.C. Tardelli, A.C. dos Reis, F. Almeraya-Calderón, P. Leo, Passive layers and corrosion resistance of biomedical Ti-6Al-4V and  $\beta$ -Ti alloys, *Coatings* 11 (2021) 487, <https://doi.org/10.3390/coatings11050487>.
- [2] K. Apaza-Bedoya, M. Tarce, C.A.M. Benfatti, B. Henriques, M.T. Mathew, W. Teughels, J.C.M. Souza, Synergistic interactions between corrosion and wear at titanium-based dental implant connections: a scoping review, *J. Periodo Res.* 52 (2017) 946–954, <https://doi.org/10.1111/jre.12469>.
- [3] J.M. Cordeiro, V.A.R. Barão, Is there scientific evidence favoring the substitution of commercially pure titanium with titanium alloys for the manufacture of dental implants? *Mater. Sci. Eng. C* 71 (2017) 1201–1215, <https://doi.org/10.1016/j.msec.2016.10.025>.
- [4] J.C. Avelar-Batista Wilson, S. Banfield, J. Housden, C. Olivero, P. Chapon, On the response of Ti-6Al-4V and Ti-6Al-7Nb alloys to a Nitron-100 treatment, *Surf. Coat. Technol.* 260 (2014) 335–346, <https://doi.org/10.1016/j.surfcoat.2014.11.034>.
- [5] M. Noronha Oliveira, W.V.H. Schunemann, M.T. Mathew, B. Henriques, R. S. Magini, W. Teughels, J.C.M. Souza, Can degradation products released from dental implants affect peri-implant tissues? *J. Periodo Res* 53 (2018) 1–11, <https://doi.org/10.1111/jre.12479>.
- [6] L.O. Berbel, E. do, P. Banczek, I.K. Karousis, G.A. Kotsakis, I. Costa, Determinants of corrosion resistance of Ti-6Al-4V alloy dental implants in an In Vitro model of peri-implant inflammation, *PLoS One* 14 (2019), e0210530, <https://doi.org/10.1371/journal.pone.0210530>.
- [7] J.C.M. Souza, K. Apaza-Bedoya, C.A.M. Benfatti, F.S. Silva, B. Henriques, A comprehensive review on the corrosion pathways of titanium dental implants and their biological adverse effects, *Metals* 10 (2020) 1272, <https://doi.org/10.3390/met10091272>.
- [8] F.N. Barrak, S. Li, A.M. Muntane, J.R. Jones, Particle release from implantoplasty of dental implants and impact on cells, *Int J. Implant Dent.* 6 (2020) 50, <https://doi.org/10.1186/s40729-020-00247-1>.
- [9] X. Chen, K. Shah, S. Dong, L. Peterson, E. Callagon La Plante, G. Sant, Elucidating the corrosion-related degradation mechanisms of a Ti-6Al-4V dental implant, *Dent. Mater.* 36 (2020) 431–441, <https://doi.org/10.1016/j.dental.2020.01.008>.
- [10] G.O. Alrabeah, P. Brett, J.C. Knowles, H. Petridis, The effect of metal ions released from different dental implant-abutment couples on osteoblast function and secretion of bone resorbing mediators, *J. Dent.* 66 (2017) 91–101, <https://doi.org/10.1016/j.jdent.2017.08.002>.
- [11] R. Delgado-Ruiz, G. Romanos, Potential causes of titanium particle and ion release in implant dentistry: a systematic review, *IJMS* 19 (2018) 3585, <https://doi.org/10.3390/ijms19113585>.
- [12] R. Bertolini, S. Bruschi, A. Bordin, A. Ghiotti, L. Pezzato, M. Dabalà, Fretting corrosion behavior of additive manufactured and cryogenic-machined Ti6Al4V for biomedical applications: fretting corrosion behavior of cryogenic machined Ti6Al4V, *Adv. Eng. Mater.* 19 (2017), 1500629, <https://doi.org/10.1002/adem.201500629>.
- [13] S. Noubissi, A. Scarano, S. Gupta, A literature review study on atomic ions dissolution of titanium and its alloys in implant dentistry, *Materials* 12 (2019) 368, <https://doi.org/10.3390/ma12030368>.
- [14] R. Bertolini, S. Bruschi, A. Ghiotti, L. Pezzato, M. Dabalà, Influence of the machining cooling strategies on the dental tribocorrosion behaviour of wrought and additive manufactured Ti6Al4V, *Biotribology* 11 (2017) 60–68, <https://doi.org/10.1016/j.biotri.2017.03.002>.
- [15] G.S. Duffó, E.Q. Castillo, Development of an artificial saliva solution for studying the corrosion behavior of dental alloys, *Corrosion* 60 (2004) 594–602, <https://doi.org/10.5006/1.3287764>.
- [16] H.M. Hamza, K.M. Deen, W. Haider, Microstructural examination and corrosion behavior of selective laser melted and conventionally manufactured Ti6Al4V for dental applications, *Mater. Sci. Eng. C* 113 (2020), 110980, <https://doi.org/10.1016/j.msec.2020.110980>.
- [17] I. Milošev, M. Metikoš-Huković, H.-H. Strehblow, Passive film on orthopaedic TiAlV alloy formed in physiological solution investigated by X-ray photoelectron spectroscopy, *Biomaterials* 21 (2000) 2103–2113, [https://doi.org/10.1016/S0142-9612\(00\)00145-9](https://doi.org/10.1016/S0142-9612(00)00145-9).
- [18] Q. Qu, L. Wang, Y. Chen, L. Li, Y. He, Z. Ding, Corrosion behavior of titanium in artificial saliva by lactic acid, *Materials* 7 (2014) 5528–5542, <https://doi.org/10.3390/ma7085528>.
- [19] M. Wang, Y. Wu, S. Lu, T. Chen, Y. Zhao, H. Chen, Z. Tang, Fabrication and characterization of selective laser melting printed Ti-6Al-4V alloys subjected to heat treatment for customized implants design, *Prog. Nat. Sci. Mater. Int.* 26 (2016) 671–677, <https://doi.org/10.1016/j.pnsc.2016.12.006>.
- [20] C.V. Funch, K. Somlo, K. Poullos, S. Mohanty, M.A.J. Somers, T.L. Christiansen, The influence of microstructure on mechanical properties of SLM 3D printed Ti-6Al-4V, *MATEC Web Conf.* 321 (2020) 03005, <https://doi.org/10.1051/mateconf/202032103005>.
- [21] A. Attanasio, M. Gelfi, A. Pola, E. Ceretti, C. Giardini, Influence of material microstructures in micromilling of Ti6Al4V alloy, *Materials* 6 (2013) 4268–4283, <https://doi.org/10.3390/ma6094268>.
- [22] M. Shahsavari, A. Imani, R.F. Schaller, E. Asselin, Corrosion evaluation of Ti-6Al-4V manufactured by electron beam melting in Ringer's physiological solution: an in vitro study of the passive film, *J. Appl. Electrochem.* (2022), <https://doi.org/10.1007/s10800-022-01683-0>.
- [23] M. Atapour, A. Pilchak, G.S. Frankel, J.C. Williams, M.H. Fathi, M. Shamanian, Corrosion behavior of Ti-6Al-4V with different thermomechanical treatments and microstructures, *065004-065004-9, CORROSION* 66 (2010), <https://doi.org/10.5006/1.3452400>.
- [24] S. Pal, M. Finsgar, T. Bončina, G. Lojen, T. Brajljih, I. Drstvenšek, Effect of surface powder particles and morphologies on corrosion of Ti-6Al-4 V fabricated with different energy densities in selective laser melting, *Mater. Des.* 211 (2021), 110184, <https://doi.org/10.1016/j.matdes.2021.110184>.
- [25] M. Motyka, Martensite formation and decomposition during traditional and AM processing of two-phase titanium alloys—an overview, *Metals* 11 (2021) 481, <https://doi.org/10.3390/met11030481>.
- [26] L.E. Murr, S.A. Quinones, S.M. Gaytan, M.I. Lopez, A. Rodela, E.Y. Martinez, D. H. Hernandez, E. Martinez, F. Medina, R.B. Wicker, Microstructure and mechanical behavior of Ti-6Al-4V produced by rapid-layer manufacturing, for biomedical applications, *J. Mech. Behav. Biomed. Mater.* 2 (2009) 20–32, <https://doi.org/10.1016/j.jmbmb.2008.05.004>.
- [27] V. Dehnavi, J.D. Henderson, C. Dharmendra, B.S. Amirkhiz, D.W. Shoesmith, J. J. Noël, M. Mohammadi, Corrosion behaviour of electron beam melted Ti6Al4V: effects of microstructural variation, *J. Electrochem. Soc.* 167 (2020), 131505, <https://doi.org/10.1149/1945-7111/abb9d1>.
- [28] J. Yang, H. Yu, J. Yin, M. Gao, Z. Wang, X. Zeng, Formation and control of martensite in Ti-6Al-4V alloy produced by selective laser melting, *Mater. Des.* 108 (2016) 308–318, <https://doi.org/10.1016/j.matdes.2016.06.117>.
- [29] M. Aziz-Kerzoo, K.G. Conroy, A.M. Fenelon, S.T. Farrell, C.B. Breslin, Electrochemical studies on the stability and corrosion resistance of titanium-based implant materials, *Biomaterials* 22 (2001) 1531–1539, [https://doi.org/10.1016/S0142-9612\(00\)00309-4](https://doi.org/10.1016/S0142-9612(00)00309-4).
- [30] I.C. Lavos-Valereto, S. Wolynec, I. Ramirez, A.C. Guastaldi, I. Costa, Electrochemical impedance spectroscopy characterization of passive film formed on implant Ti-6Al-7Nb alloy in Hank's solution, *J. Mater. Sci. Mater. Med.* 15 (2004) 55–59, <https://doi.org/10.1023/B:JMSM.0000010097.86245.74>.
- [31] J.E.G. González, J.C. Mirza-Rosca, Study of the corrosion behavior of titanium and some of its alloys for biomedical and dental implant applications, *J. Electroanal. Chem.* 471 (1999) 109–115, [https://doi.org/10.1016/S0022-0728\(99\)00260-0](https://doi.org/10.1016/S0022-0728(99)00260-0).
- [32] D. Kek-Merl, J. Lappalainen, H.L. Tuller, Electrical properties of nanocrystalline CeO[sub 2] thin films deposited by in situ pulsed laser deposition, *J. Electrochem. Soc.* 153 (2006) J15, <https://doi.org/10.1149/1.2165778>.
- [33] S. Marinel, D.H. Choi, R. Heuguet, D. Agrawal, M. Lanagan, Broadband dielectric characterization of TiO<sub>2</sub> ceramics sintered through microwave and conventional processes, *Ceram. Int.* 39 (2013) 299–306, <https://doi.org/10.1016/j.ceramint.2012.06.025>.
- [34] M.C. Biesinger, L.W.M. Lau, A.R. Gerson, R.St.C. Smart, Resolving surface chemical states in XPS analysis of first row transition metals, oxides and hydroxides: Sc, Ti, V, Cu and Zn, *Appl. Surf. Sci.* 257 (2010) 887–898, <https://doi.org/10.1016/j.apusc.2010.07.086>.
- [35] J. Fojt, M. Fousova, E. Jablonska, L. Joska, V. Hybasek, E. Pruchova, D. Vojtech, T. Ruml, Corrosion behaviour and cell interaction of Ti-6Al-4V alloy prepared by two techniques of 3D printing, *Mater. Sci. Eng. C* 93 (2018) 911–920, <https://doi.org/10.1016/j.msec.2018.08.066>.
- [36] J.F. Moulder, W.F. Stickle, P.E. Sobol, K.D. Bomben, J. Chastain, R.C. King Jr., Physical electronics, incorporation. Handbook of X-Ray Photoelectron Spectroscopy: A Reference Book of Standard Spectra for Identification and Interpretation Of XPS Data, Physical Electronics, Eden Prairie, Minn., 1995.
- [37] S. Saketi, J. Östby, U. Bexell, M. Olsson, A methodology to systematically investigate the diffusion degradation of cemented carbide during machining of a titanium alloy, *Materials* 12 (2019) 2271, <https://doi.org/10.3390/ma12142271>.

- [38] J. Pimenta, S. Szmukler-Moncler, A.J. Raigrodski, Physical characterization of 3 implant systems made of distinct materials with distinct surfaces, S0022391320307289, *J. Prosthet. Dent.* (2021), <https://doi.org/10.1016/j.prosdent.2020.11.015>.
- [39] L. Crespo, M. Hierro-Oliva, S. Barriuso, V. Vadillo-Rodríguez, M.Á. Montealegre, L. Saldaña, E. Gomez-Barrena, J.L. González-Carrasco, M.L. González-Martín, N. Vilaboa, On the interactions of human bone cells with Ti6Al4V thermally oxidized by means of laser shock processing, *Biomed. Mater.* 11 (2016), 015009, <https://doi.org/10.1088/1748-6041/11/1/015009>.
- [40] E.D. Giglio, C.D. Calvano, I. Losito, L. Sabbatini, P.G. Zambonin, A. Torrisi, A. Licciardello, Surface (XPS, SIMS) chemical investigation on poly(pyrrrole-3-acetic acid) films electrosynthesized on Ti and TiAlV substrates for the development of new bioactive substrates, *Surf. Interface Anal.* 37 (2005) 580–586, <https://doi.org/10.1002/sia.2053>.
- [41] M. Pourbaix, *Atlas of Electrochemical Equilibria in Aqueous Solutions*, National Assoc. of Corrosion Engineers [u.a.], Houston, Tex, 1974.
- [42] A.A. El Sawy, M.A. Shaarawy, Evaluation of metal ion release from Ti6Al4V and Co-Cr-Mo casting alloys: in vivo and in vitro study: metal ion release from Ti6Al4V and Co-Cr-Mo casting alloys, *J. Prosthodont.* 23 (2014) 89–97, <https://doi.org/10.1111/jopr.12067>.
- [43] I. Milošev, B. Kapun, V.S. Selih, The effect of fluoride ions on the corrosion behaviour of Ti metal, and Ti6-Al-7Nb and Ti-6Al-4V alloys in artificial saliva, *Acta Chim. Slov.* 60 (2013) 543–555.
- [44] H. Zhang, C. Man, C. Dong, L. Wang, W. Li, D. Kong, L. Wang, X. Wang, The corrosion behavior of Ti6Al4V fabricated by selective laser melting in the artificial saliva with different fluoride concentrations and pH values, *Corros. Sci.* 179 (2021), 109097, <https://doi.org/10.1016/j.corsci.2020.109097>.
- [45] H.K. Joanna Locha, Influence of fluoride ions in artificial saliva solution to corrosion behavior of Ti-6Al-4V and Ti-10Mo-4Zr titanium alloys, *J. Cast. Mater. Eng.* 2 (2018) 5, <https://doi.org/10.7494/jcme.2018.2.3.57>.